Valence instability and collapse of ferromagnetism in EuB_6 at high pressures

L. O. Kutelak[a,b], R. Sereika[c], G. Fabbris[d], L. Francisco[a,b], G. Lombardi[a,b], E. H. T. Poldi[a,b], J. Zhao[d], E. E. Alp[d], N. M. Souza Neto[a], P. F. S. Rosa[e], D. Haskel[d], W. Bi[c], R. D. dos Reis[a]

[a]*Brazilian Synchrotron Light Laboratory (LNLS) Brazilian Center for Research in Energy and Materials (CNPEM) Campinas Sao Paulo Brazil*
[b]*Instituto de Fisica Gleb Wataghin Universidade Estadual de Campinas (UNICAMP) SP Brazil*
[c]*Department of Physics University of Alabama at Birmingham Birmingham AL 35294 USA*
[d]*Advanced Photon Source Argonne National Laboratory Argonne Illinois 60439 USA*
[e]*Los Alamos National Laboratory - Los Alamos NM 87545 USA*

Abstract

Despite the simplicity of their cubic crystal lattice, rare-earth hexaborides display complex physical properties including a (long debated) onset of metallization via magnetic polaron formation at $T_{c1} \approx 15$ K preceding ferromagnetic ordering at $T_{c2} \approx 12$ K. In this work, we used applied pressure to tune the interplay between electronic structure and magnetism in EuB_6. We probed the magnetism, valence, and structure of EuB_6 under quasi-hydrostatic pressures up to 30 GPa using X-ray techniques. Our findings show evidence for collapse of ferromagnetism above 20 GPa following a monotonic increase of mean Eu valence. While X-ray diffraction measurements in the paramagnetic state at room temperature show that the lattice retains cubic symmetry, a measurable quadrupole interaction seen by time-domain synchrotron Mössbauer spectroscopy suggests a lowering of symmetry associated with magnetic ordering, becoming more prominent across the magnetic transition. The interplay between conduction band electron count and magnetism observed under applied pressure in EuB_6 opens possibilities for fine-tuning metallization and magnetic properties of similar Eu-based semi-metal systems.

1. Introduction

EuB_6 is the representative ferromagnetic member within the family of rare-earth hexaborides, which exhibits a plethora of puzzling transport, magnetic and topological properties such as the proposed topological Kondo insulator behavior [1, 2, 3, 4, 5, 6, 7, 8, 9, 10, 11, 12, 13, 14, 15]. EuB_6 has a long history of experimental puzzles, such as the two-step transition at $T_{c1} = 15.3$ K and $T_{c2} = 12.5$ K. Initially, it was believed that T_{c1} originated from magnetic ordering, while T_{c2} occurred due to a reorientation of the magnetization direction [16]. Later, it was argued that the higher temperature transition is attributed to the material's metallization through the overlap of magnetic polarons, resulting in $T_{c2} = 12.5$ K as the actual magnetic ordering temperature [17], which is in agreement with T_c obtained by neutron diffraction [18]. Further evidence for

Email address: ricardo.reis@lnls.br (R. D. dos Reis)

magnetic polarons has been reported by scanning tunneling microscopy [19], magneto optical imaging [20], Raman scattering [21], and magnetoresistance [22]. Experiments with Yb doping further supports the separation between magnetic ordering and metallization [23] suggesting polaron overlap and subsequent magnetic ordering is the most likely scenario.

Recently it was suggested that non-trivial topological phases may arise in special conditions of magnetization direction as long as specific mirror symmetries are conserved [24, 25, 26]. A change in magnetization direction may turn EuB_6 from a topological nodal-line semiconductor to a Weyl semimetal [24]. Compressing the lattice while conserving crystal structure using hydrostatic pressure is a convenient route to tune magnetic and electronic properties which might generate changes in topology.

High pressure electrical resistivity experiments showed an increase of both transition temperatures up to pressures of about 5 GPa. At higher pressures up to 17 GPa, both transition temperatures remain unchanged [27]. It is suggested that the Ruderman–Kittel–Kasuya–Yosida (RKKY) interaction is responsible for the magnetism of the sample, with electronic density at the X point of the Brillouin zone, which hosts electron and hole pockets [28, 29], playing a main role for the changes in the interaction. Notably, carbon doping turns EuB_6 into an antiferromagnet [30] and band structure calculations of pure EuB_6 reveal the presence of two effective exchange couplings between $4f$ moments and itinerant electrons: a parallel (ferromagnetic) coupling to conduction electrons and an antiparallel (antiferromagnetic) coupling to valence electrons [31].

Applied hydrostatic pressure is a clean, symmetry-preserving tuning parameter that not only provides information about the evolution of magnetic phases but also holds the promise to unveil new emergent phenomena. The simple cubic structure ($Pm\bar{3}m$) seems ideal for hydrostatic pressure experiments with evidence for structural sturdiness in CeB_6, which shares the same structure and shows no structural transitions up to at least 85 GPa of applied pressure [32]. In this work, quasi-hydrostatic pressures to 30 GPa were applied to high-quality Al-flux grown samples of EuB_6 [33, 34], in which single crystals were mechanically crushed into powdered form. We utilized a range of synchrotron techniques including X-ray absorption near edge spectroscopy (XANES), X-ray magnetic circular dichroism (XMCD), X-ray diffraction (XRD) and time-domain synchrotron Mössbauer spectroscopy (SMS), to shed light into the electronic ground state of EuB_6 under high pressures and low temperatures. The experimental data gathered provide insights into the evolution of electronic and magnetic properties such as an observed increase in mean valence above 10 GPa and collapse of ferromagnetic ordering at 20 GPa, with likely emergence of antiferromagnetic order at higher pressures. Additionally, the observation of a non-zero quadrupole interaction in the SMS data at low temperatures is indicative of lowering of point symmetry at Eu sites which becomes more pronounced above the magnetic transition.

2. Methods

Single-crystal samples were grown from Al flux as described in Ref. [35, 36]. For the different experiments, samples were always selected from the same batch. XANES and XMCD measurements were performed at the 4ID-D beamline [37] of the Advanced Photon Source (APS), Argonne National Laboratory. EuB_6 single crystals were crushed into fine powder and placed inside a miniature diamond anvil cell (DAC) within a laser drilled [38] rhenium gasket for sample support together with silicone oil as pressure transmitting medium. A helium-flow cryostat was used for controlling the sample temperature down to 6 K. Each pressure point was obtained by removing the sample from the cryostat and applying torque at room temperature to the DAC screws. Pressure was measured at room temperature before and after each data collection cycle

with the Ruby fluorescence technique [39]. For XMCD experiments, a quarter wave plate was used to generate circularly polarized X-rays of alternating helicity. XMCD data were collected in helicity-switching mode in fixed magnetic field direction. Data were collected in magnetic field up to 4 T applied either along or opposite to the X-ray helicity direction. The redundant reversal of X-ray helicity and magnetic field allows us to rule out artifacts of non-magnetic origin in the XMCD signals. Both XANES and XMCD data were normalized by the difference between post-edge and pre-edge absorption to account for any sample thickness change in the pressure cell at the different applied pressures.

Room temperature X-ray diffraction was performed at the EMA beamline of the Brazilian Synchrotron Light Laboratory, Sirius. A fine powder sample was obtained from single crystals and placed inside a rhenium gasket while utilizing neon gas as pressure medium. A ruby sphere was placed together with sample for pressure measurement and a standard DAC coupled to a gas-membrane system was utilized for pressure application. The X-ray energy was calibrated to a 0.4859 Å wavelength and the beam focused with a KB mirror pair to a 20×20 μm^2 focus size at the sample position. The diffraction patterns were then detected with a marCCD mosaic 220. DIOPTAS [40] software was utilized to integrate 2θ intensities from diffraction rings which were limited to an 120 degrees azimuth due to the experiment geometry and CCD placement. More details on the XRD measurements and data analysis are included in the Supplemental Material (SM) [41].

The time-domain synchrotron Mössbauer spectroscopy measurements were performed at the 3ID-B beamline of the APS at the Argonne National Laboratory, using EuB_6 crystals inside a mini-panoramic DAC [42] with helium gas as pressure transmitting media inside the laser-drilled rhenium gasket. The helium flow cryostat base temperature for the SMS measurements was 9 K which is below T_c for EuB_6. The combination of a helium gas membrane and on-line ruby fluorescence detection allowed for in-situ control of pressure at low temperature.

3. Results

The pressure dependence of the Eu valence at T = 6 K was determined using the element and orbital selectivity of X-ray absorption spectroscopy. Results for selected pressure points for the Eu- L_3 absorption edge are shown in Fig. 1. For pressures up to 10 GPa there is only one absorption peak, which is associated with the Eu^{2+} valence. For higher pressures, a shoulder is observed about 8 eV above the L_3 absorption peak (white line), which suggests that the mean valence of Eu is shifting towards a 3+ state in a systematic manner as shown in the inset of Fig. 1. To accurately estimate the Eu valence, we utilized the Finite Difference Method Near Edge Structure (FDMNES) code [43] to perform first principle calculations of the XANES spectra for both Eu valence configurations (2+ and 3+) using the lattice parameters determined by XRD. Then, the theoretical Eu^{2+} and Eu^{3+} XANES spectra were linearly combined to reconstruct the experimental data [44, 45]. This method takes into account the different shape of XANES spectra for each of the valence states (further details of this method are included in the SM [41]). Accounting for the different ratio of white line to edge jump for the two valence states it was possible to estimate that the Eu^{3+} contribution at 15 GPa is 2% and reaches 9% at 28.5 GPa. This corresponds to an average valence increase from 2+ at ambient pressure to 2.09+ at 28.5 GPa. This indicates that magnetic Eu^{2+} and non-magnetic Eu^{3+} states coexist in the material. A data point collected after pressure release from 28.5 GPa to 15.3 GPa indicates that the valence change appears to be reversible because the observed satellite peak from Eu^{3+} diminishes in intensity.

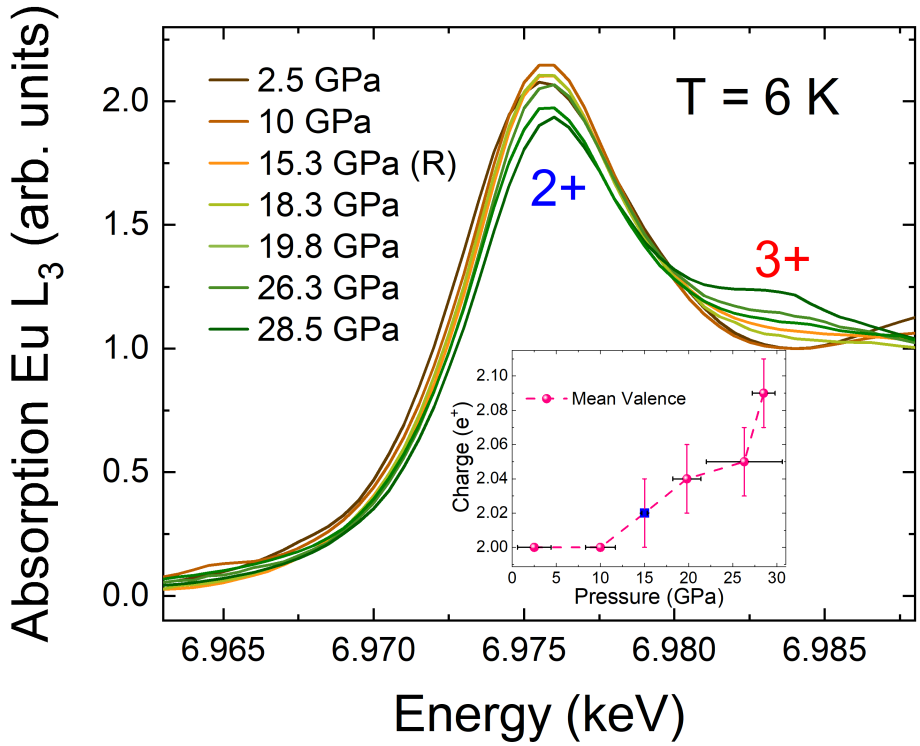

Figure 1: Eu-L_3 XANES spectra for selected pressure points at 6 K. We observe only one peak at the Eu L_3 edge up to 10.3 GPa associated with a pure 2+ valence state. At higher pressures, a kink around 8 eV above the main peak appears and grows with pressure. Inset shows the valence evolution as a function of pressure obtained by adjusting simulated spectra with experimental data. Simulated data is available in the Supplemental Material [41]. Data point at 15.3 GPa was taken after releasing the pressure from 28.5 GPa.

Although XANES results strongly suggest that the Eu mean valence increases under applied pressure, a change in structural symmetry and related changes in X-ray absorption fine structure could also cause the appearance of the second absorption peak [46]. To verify the stability of the structure over this pressure range we performed in-situ high pressure synchrotron X-ray powder diffraction up to 30 GPa at ambient temperature. The X-ray difractograms, presented in the SM [41], do not reveal the presence of extra peaks over the entire pressure range studied, indicating that no structural phase transition takes place up to the highest pressure at ambient temperature. It is worth noting that subtle structural changes may take place at low temperature below the magnetic ordering temperature, as pointed out by magnetostriction measurements [22] and Raman measurements [47]. The lack of structural transitions at ambient temperature and the systematic, gradual increase in mean valence over a 20 GPa range, indicate that the changes seen in XANES are associated with a valence evolution and not with a change in atomic arrangement around the Eu absorbing ions. The GSAS-II [48] software was used to perform Le-Bail analysis of our powder diffraction data to obtain the unit cell volume for each of the pressures, which are shown in Fig. 2. It was then possible to fit the derived volumes to a third order Birch-Murnaghan equation of state [32] where the initial volume V_0 was set as a fit parameter because our first pressure point was 1.5 GPa. The best fit of our data provided $B_0 = 139 \pm 2$ GPa, $B_0^{'} = 4.1 \pm 0.2$ and $V_0 = 73.80 \pm 0.04$ Å^3, which is consistent with the recently reported value of $B_0 = 141.0 \pm 0.9$ GPa [49]. These experimental values differ by about 16% from theoretical values of $B_0 = 161$ GPa [31], and $B_0 = 152.4$ GPa and $B_0^{'} = 3.59$ [26].

Because of the valence instability, one might expect changes in the magnetic behavior of the material. Here we used the spin-dependent sensitivity and atomic selectivity of XMCD to probe the magnetic properties of Eu. XMCD spectra probe the empty spin-dependent density of states (DOS) near the Fermi level, as opposed to the spin-averaged empty DOS probed by XANES. Fig. 3 presents the XMCD spectra at the Eu L_3-edge as a function of applied pressure. XMCD data were obtained with an applied magnetic field H = 4 T for all spectra except 2.5 GPa and 10 GPa where H = 1 T was applied. It is worth noting that, as shown by XMCD as function of applied field in Fig. S5 available in the SM [41], magnetization is nearly saturated at 1 T. It is clear that for pressures up to 18.4 GPa there is a dichroic signal. However, at 19.8 GPa a significant drop of XMCD signal is observed and the signal vanishes at 28.5 GPa. The vanishing of XMCD signal indicates loss of net spin polarization in the $5d$ states, namely, vanishing of net magnetization. However, as XMCD only probes the net magnetization, the collapse of XMCD can indicate that the material becomes either antiferromagnetic or paramagnetic. We note that, similarly to what happens for the valence in XANES experiments, when the pressure is released to 10 GPa the XMCD is restored, demonstrating that the transition is reversible.

In order to investigate further the changes in valence and magnetic order time-domain synchrotron Mösssbauer Spectroscopy was used to better understand magnetic and electronic characteristics of our sample at high pressures. Mösssbauer spectroscopy relies on the absorption and (delayed) emission of radiation by nuclei of certain isotopes, Eu-151 being one of them. Eu-151 has a 21.54 keV transition between a I = $\frac{7}{2}$ excited state and I = $\frac{5}{2}$ ground state, where I is nuclear spin [50]. Here, we analyze the delayed (half-life $\tau = 9.7$ ns) X-ray emission of Eu nuclei decaying into the ground state. Because nuclear levels split and display hyperfine structure under the influence of magnetic field, and because the emission from transitions between excited and ground split levels is coherent, interference leads to quantum beats in the delayed X-ray emission. Because one can probe Zeeman split nuclear levels, it is possible to determine whether the sample is under the influence of an internal magnetic field. As shown in Fig. 4 a well-defined interference pattern due to quantum beats coming from magnetically split nu-

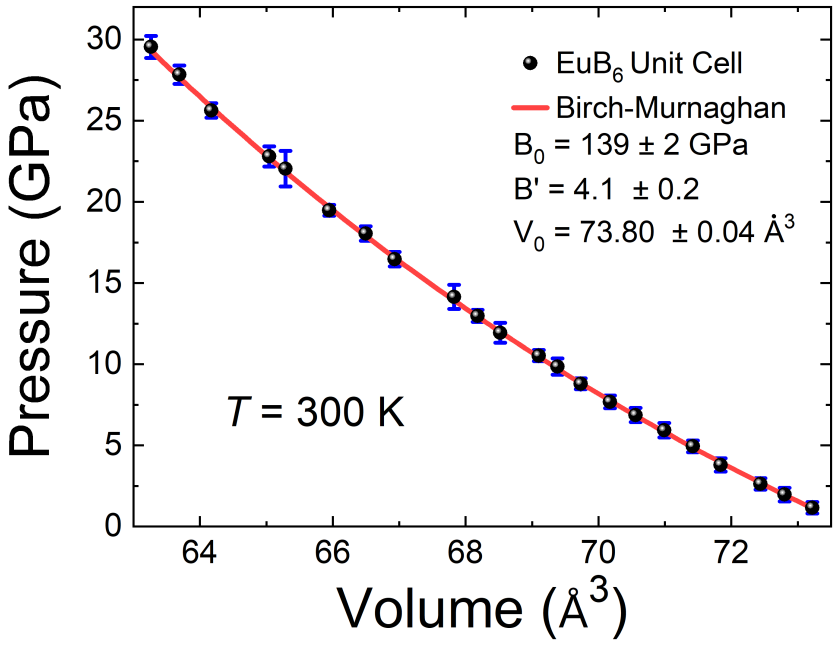

Figure 2: Applied pressure as a function of unit cell volume for EuB_6. Uncertainties for cell volume are smaller than the points. Red line indicates the fitted curve for a third-order Birch-Murnaghan equation of state.

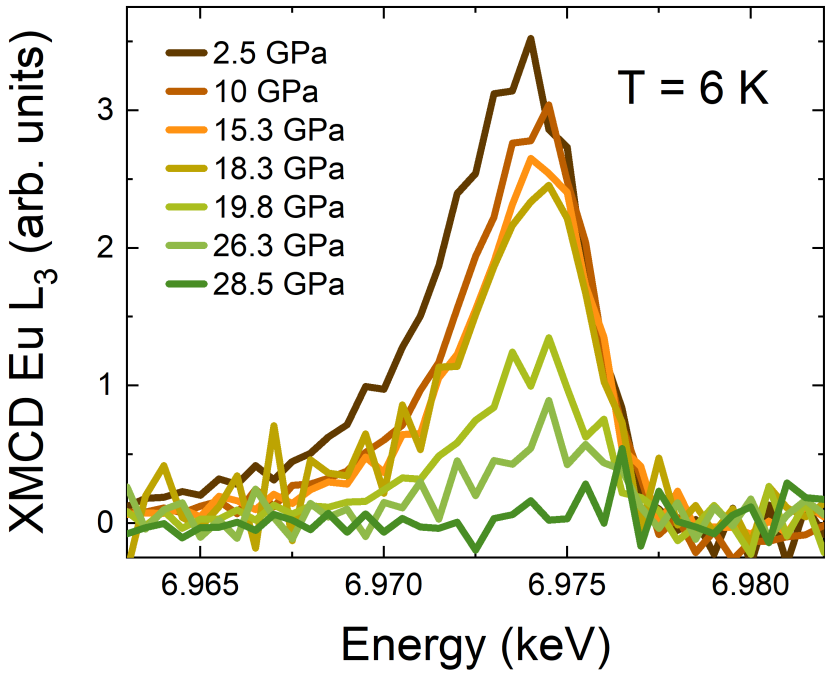

Figure 3: X-Ray magnetic circular dichroism spectra for Eu L_3 absorption edge for selected pressure points at T = 6 K. While a prominent XMCD signal is observed up to 18.3 GPa, the XMCD is suddenly suppressed above that pressure and no XMCD is detected at 28.5 GPa.

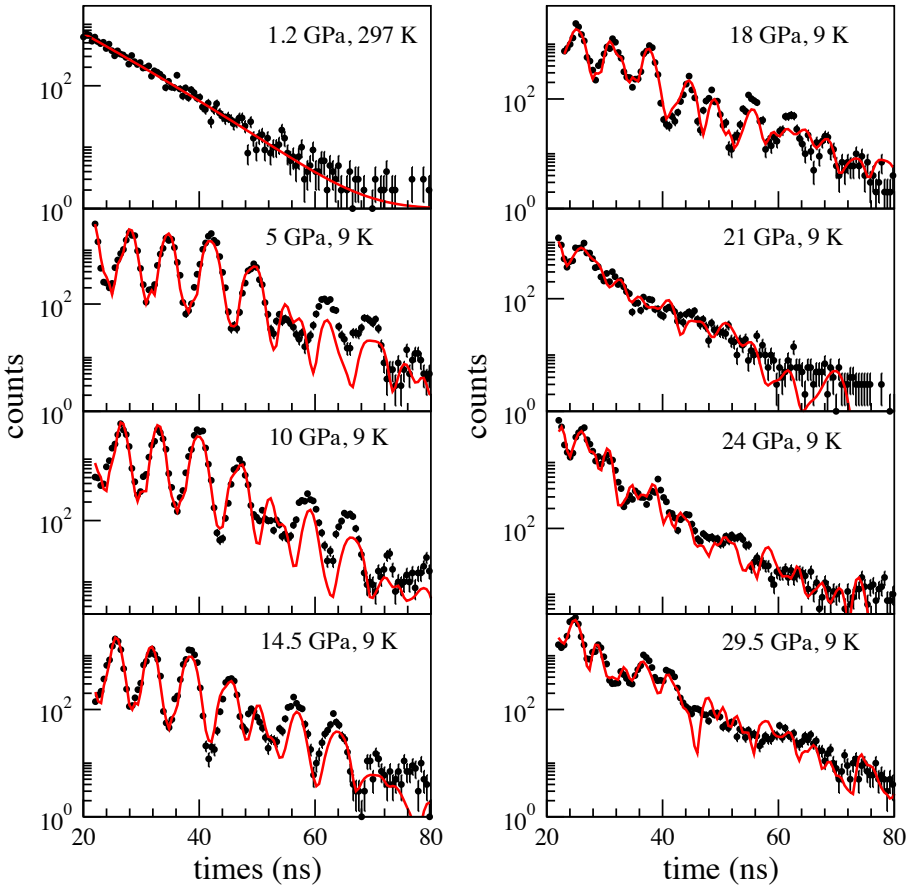

Figure 4: SMS experimental data (black points) and fits (red lines) using models described in the main text. Fitted hyperfine interaction parameters for the low temperature data are shown in Fig. 5

clear Zeeman levels is observed between 5 GPa and 18 GPa. Notably, a dramatic change in quantum beat behavior emerges at higher pressures. At 21 GPa, a major difference in the time domain spectra is observed, where the beating due to magnetic splitting appears to be severely suppressed. This results indicate a change in the hyperfine field , in agreement with XMCD data. We note that this hyperfine field arises from three main contributions: the core electron polarization, the polarization of conduction electrons by Europium's electrons, and the polarization of conduction electrons by neighboring atoms [51]. The strong suppression of the hyperfine field at the magnetic transition may be a result of frustration from competing FM and AFM exchange interactions at the critical pressure, resulting in a magnetically disordered phase. For pressures of 24 GPa and 30 GPa quantum beats reappear in the SMS spectra. The possible origin of these quantum beats is discussed below.

Analysis of the time domain spectra was performed utilizing the CONUSS [52] software. SMS

fits are also shown in Fig. 4. For data up to 14.5 GPa the fits describe quantum beats reasonably well for almost the entire range of time delays, with exceptions at higher delayed emission times. This is in agreement with the previously reported ferromagnetic behavior of EuB_6 up to these pressures at 9 K [27] and also with our XMCD measurements.

For data at higher pressures, two main models were tested: Model 1 in which EuB_6 becomes antiferromagnetic for pressures higher than 21 GPa, and Model 2, where EuB_6 would become paramagnetic above 21 GPa, with the internal magnetic field strength severely diminished. The fits for Model 1 are depicted in Fig. 4, fits for Model 2 and simulated energy domain spectra equivalent to the time domain SMS spectra for Model 1 are presented in the SM Fig. S12 and S15 respectively [41]. Our model also provides the hyperfine field and quadrupole interaction (QI) eQV_{zz} (where e is the proton charge, Q the nuclear quadrupole moment in the ground state and V_{zz} principal component of the electric field gradient) as function of applied pressure, as shown in Fig. 5. The hyperfine field increases linearly from about 29.1 T at 5 GPa to 33 T at 20 GPa. The low pressure value of the hyperfine field is in reasonable agreement with the reported ambient pressure value of B_{HF}=26.2 T (T=4.2 K) in an EuB_6 single crystal [53]. There is then a decrease in hyperfine field in the 18-21 GPa range, of about 30%, followed by a slight increase to 25.6 T at 29.5 GPa. The sudden change in hyperfine field appears to correlate with the disappearance of ferromagnetic order seen in the XMCD data. The QI follows a different trend, starting with a value of 2.7 mm/s at 5 GPa and exhibiting an increase up to 21 GPa. The change in QI appears to correlate more closely with the change in mean valence. It is worth noting that above 21 GPa, the experimental data shows suppressed features and faint beats. From the analysis, we argue that EuB_6 may undergo a magnetic transition from ferromagnetic to antiferromagnetic ordering with lattice contraction, as expected for a metal with RKKY interactions where the exchange coupling between Eu ions depends on interatomic distance and Fermi surface dimensions. Although Model 2 also presents reasonable agreement with experimental data, it would require a rather unphysical strong QI ranging from 43 mm/s up to 45 mm/s. Such a giant QI was reported previously in some Eu compounds such as $EuRh_3B_2$ [54, 55], but it is unlikely to occur in EuB_6 because it has a room temperature cubic structure in the $Pm\bar{3}m$ space group with Eu $\bar{3}m$ point symmetry which is unlikely to generate strongly non-spherical distribution for the electric charge around the Eu nuclei. We also note that the Eu-Eu spacing in EuB_6 is much larger (approximately 4 Å) compared to $EuRh_3B_2$ (2 Å). More details about Model 2 are provided in the SM[41]. As mentioned earlier, subtle structural distortions and lowering of Eu point symmetry associated with magnetic ordering are likely to occur in EuB_6 at low temperatures, giving rise to finite QI values also in Model 1. SMS at 1.2 GPa and 297 K in the high temperature, paramagnetic phase (Fig. 4) shows a linear decay without quantum beats indicating negligible QI as a result of cubic point symmetry.

4. Discussion

The combination of XAS and XRD enables the assignment of the changes in XAS under pressure to changes in Eu valence. Specifically, EuB_6 enters a phase where Eu^{2+} and Eu^{3+} coexist above about 10 GPa. The time scale of the XAS measurement is dictated by the $2p_{3/2}$ core-hole lifetime, of about 10^{-16} sec. The typical time scale of fluctuating valence between $4f^7$ and $4f^6$ states is about 10^{-11} sec [56, 44]. XAS time scale being faster than valence fluctuation rates, it cannot distinguish between a static distribution of inequivalent 2+ and 3+ Eu sites, and a single Eu site with fluctuating valence (XAS measures the two components separately as they are separate in absorption energy). Since Eu^{3+} ions are much smaller than Eu^{2+} ions, the scenario

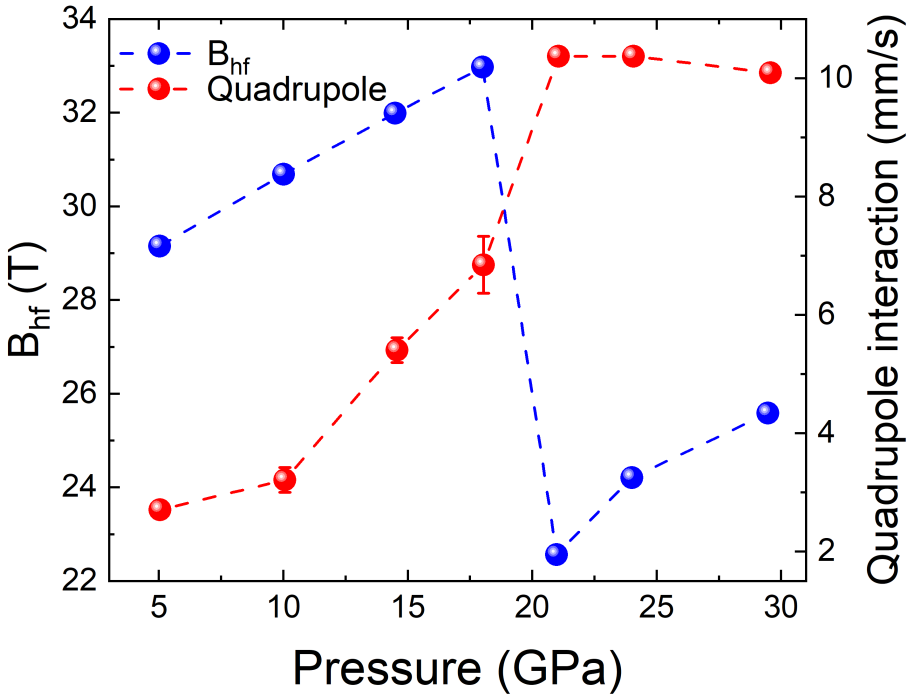

Figure 5: Pressure evolution of magnetic hyperfine field (left axis) and quadrupole interaction (right axis) as obtained with SMS spectra fitting. It is possible to see a clear change in behavior for both parameters at the 18 GPa mark where B_{hf} decreases while QI sharply increases. Uncertainties for pressures are smaller than the symbols.

with two inequivalent sites would typically require a crystal structure modification or lattice anomalies. In our XRD data, no structural transition or lattice anomaly is observed which makes this possibility highly unlikely. On the other hand, in most divalent Eu compounds, pressure drives Eu to a spatially homogenous, fluctuating valence state [44, 57, 58]. We note that the time scale of Mössbauer spectroscopy, dictated by the half-life of the Eu-151 excited nuclear state of 10^{-8} s, is much slower than fluctuating valence rates. Therefore Mössbauer spectroscopy sees a weighted average Eu valence, while XANES will see the individual fluctuating components with their respective weights [59]. Therefore, in the analysis of time-domain SMS data, only one Eu site was used. We note that, unlike conventional Mössbauer spectroscopy, the isomer shift is not accessible in time-domain SMS experiments unless a reference sample with known valence is measured concomitantly with the EuB_6 sample, which was not done here.

To elucidate the behavior of the electron occupancy in EuB_6 we performed ab-initio DFT simulations utilizing WIEN2k package [60] following the same procedure described in ref [61]. Applied pressure was simulated by decreasing the lattice parameter following the Birch-Murnaghan equation of state, Fig. 2. Our simulations indicate that Eu 5*d* orbital occupation steadily increases while Eu 4*f* decreases as pressure is applied as shown in Table 1. While the trend is consistent with experiment, the change in 4*f* occupation is an order of magnitude smaller than the charge/valence increase seen in XANES. This difference may occur because in our DFT model the 4*f* electrons are treated as well localized core electrons, hence 4*f*-5*d* hybridization is likely to be underestimated. This charge transfer from innermost Eu 4*f* shell and B atoms to 5*d* states and interstitial space is in agreement with previous EuB_6 high pressure studies [27]. More details from our DFT analysis can be found in the SM [41].

Regarding the magnetic ordering, both XMCD and SMS results undoubtedly show that EuB_6 remains a ferromagnet up to 18 GPa, while for higher pressures there is a collapse of the ferromagnetic ordering. Our modeling of the SMS data indicates that the high pressure phase above 20 GPa hosts antiferromagnetic (AFM) ordering. Our modeling indicates that a finite QI is present at low temperature in the magnetically ordered phases, despite cubic symmetry being present at ambient temperature, likely a result of subtle lowering of lattice symmetry driven by magnetic ordering, supported by results from magnetostriction measurements [22]. Another possible source of electric field gradient is a region of valence instability coming from delocalization of charges of Eu and B atoms as suggested by RIXS measurements [62]. While our modeling cannot unambiguously rule out the presence of a paramagnetic phase above 20 GPa, the requirement for a very large, unphysical QI of about 43-45 mm/sec makes this scenario highly unlikely.

Additional evidence in support of an AFM high pressure phase comes from XMCD measurements at ambient pressure collected above the magnetic ordering temperature, i.e., in the PM state. In the PM state the applied field at low temperature induces magnetization. As shown in Fig. S5 of SM [41] , the induced magnetization at 4 T and low temperature in the uncorrelated PM state is a significant fraction of the magnetization of the ordered state, a result of the small anisotropy of the spherically symmetric $4f^7$ Eu^{2+} ions. Were the high pressure phase also be PM, we would expect a sizable induced magnetization at 4 T and low T. However, this is not observed and the magnetic susceptibility remains quite small or negligible in the high pressure phase indicative of a correlated state such as AFM. Another argument in favor of an AFM state comes from the fact that usually Eu systems present much higher valence than 2.1+ in the paramagnetic state, as observed in [63].

In addition, as also observed by Cooley *et al.* [27], despite a T_c value increase for pressures up to 5 GPa, the Curie temperature of the material remains nearly constant in the 5-20 GPa range. The consistent value of ordering temperature at higher pressures may be a result of an

Table 1: Pressure dependence of orbital occupancies from DFT calculations.

Charge site	0 GPa (e^-)	30 GPa (e^-)
Eu 5*d*	0.2255	0.3071
Eu 4*f*	6.8327	6.7962
Eu total	60.620	60.699
B total	3.455	3.377
Interstitial	11.652	12.037

interplay between changes in RKKY interaction and valence. Mixed valency under applied pressure increases mixing of 4f and conduction electrons, leading to an increase of indirect exchange coupling J, raising the magnetic ordering temperature, while a shift to non-magnetic Eu^{3+} (magnetic dilution) may act to decrease J. A similar behavior was also observed in the $Eu_{0.5}Yb_{0.5}Ga_4$ compound [61]. Further SMS measurements (shown in Fig. S13 of SM [41]) performed at T = 20 K,show the same internal field of the data at T=9 K at 29.5 GPa. This results indicate that there are no magnetic phase transitions between 9 K and 20 K, which in turn implies that EuB_6 remains in the same magnetic state in this temperature range.

While our interpretation leads us to conclude that AFM order best describes the high pressure phase, we note that this contrasts with the behavior under pressure of other magnetically ordered Eu containing compounds [64] such as $EuRh_2Si_2$ [65], $EuNi_2Si_2$ [66] and $EuCo_2Ge_2$ [67] which present valence shifting towards 3+ but go from a AFM ambient pressure state to a high pressure paramagnetic phase. Meanwhile, ambient pressure FM $EuRu_2P_2$ becomes paramagnetic at 1.5 GPa but also presents a structural transition [68], which is absent in EuB_6. While a coexistence of AFM and FM phases was previously reported in carbon doping experiments [30], such coexistence is incompatible with negligible XMCD signal in the high pressure phase. In order to provide additional evidence in favor of magnetic order in the high pressure phase, additional experimentation using high pressure resonant inelastic X-ray scattering (RIXS) and transport measurements up to 30 GPa and beyond, are highly desired.

5. Summary

In conclusion, by combining XAS, XRD and SMS experiments at pressures up to 30 GPa we demonstrate that both the magnetic ordering and the valence of the EuB_6 compound can be tuned by external pressure without an observable change in structure at room temperature. Further, by extending the pressure range over previous studies, we show an increase in the valence of Eu above about 10 GPa together with the collapse of ferromagnetism near 20 GPa. Open questions that remain include the nature of magnetic ordering in the high pressure phase, which we postulate to be AFM-type based on modeling of SMS data. Additionally, the need to include a quadrupole interaction in the modeling of SMS data indicates that the point symmetry at Eu lattice sites is lower than cubic at low temperature. Since the room temperature crystal structure is cubic at all pressures, this observation is likely a result of lowering of symmetry by magnetic order, as previously noted in magnetostriction and Raman experiments [22, 47]. That the QI not only remains but strengthens in the high pressure phase is another indication that the high pressure low temperature phase hosts magnetic ordering and point symmetry lower than cubic.

Finally, the mechanical control of magnetism and valence for EuB_6 provides a pathway for exploring the connection between magnetic order and topology in this material since the col-

lapse in magnetic order could lead to suppression of topological states [69]. Signatures of such interdependece may appear in transport and mechanism of exchange interactions both in the rare earth hexaboride family as well as in their related compounds.

ACKNOWLEDGMENTS

We acknowledge Flavio Gandra, Michael Nicklas and Cristoph Geibel for fruitful discussions. We thank the financial support from the Brazilian agencies CNPq, CAPES and FAPESP (Grants 2018/00823-0, 2018/19015-1, 2021/02314-9 and 2022/05447-2). RDdR and L.O.K acknowledges financial support from the Max Planck Society under the auspices of the Max Planck Partner Group R. D. dos Reis of the MPI for Chemical Physics of Solids, Dresden, Germany. L.F. acknowledge financial support from FAPESP grant 2018/10585-0. E.H.T.P and G.A.L acknowledge financial support from CNPq studentship grant No. 136119/2018-2 and No. 140632/2018-2 respectively. We are grateful to GSECars for the help with gas loading in SMS experiments. Work at Argonne is supported by the U.S. Department of Energy, Office of Science, Office of Basic Energy Sciences, under Contract No. DE-AC-02- 06CH11357. Work at Los Alamos National Laboratory was performed under the auspices of the U.S. Department of Energy, Office of Basic Energy Sciences, Division of Materials Science and Engineering. This research used facilities of the Brazilian Synchrotron Light Laboratory (LNLS), part of the Brazilian Center for Research in Energy and Materials (CNPEM), a private non-profit organization under the supervision of the Brazilian Ministry for Science, Technology, and Innovations (MCTI). The EMA beamline and LCTE staff are acknowledged for the assistance during the experiments 20210101. W.B. acknowledge support from the support from National Science Foundation (NSF) CAREER Award No. DMR-2045760.

References

[1] P. Coleman *et al.*, Handbook of magnetism and advanced magnetic materials (2007).
[2] M. Dzero, K. Sun, V. Galitski, and P. Coleman, Physical Review Letters **104**, 106408 (2010).
[3] K. Flachbart, S. Gabáni, K. Neumaier, Y. Paderno, V. Pavlík, E. Schuberth, and N. Shitsevalova, Physica B: Condensed Matter **378-380**, 610 (2006).
[4] N. Xu, C. E. Matt, E. Pomjakushina, X. Shi, R. S. Dhaka, N. C. Plumb, M. Radović, P. K. Biswas, D. Evtushinsky, V. Zabolotnyy, J. H. Dil, K. Conder, J. Mesot, H. Ding, and M. Shi, Physical Review B **90**, 085148 (2014).
[5] J. D. Denlinger, J. W. Allen, J.-S. Kang, K. Sun, B.-I. Min, D.-J. Kim, and Z. Fisk (Journal of the Physical Society of Japan, 2014).
[6] J. Jiang, S. Li, T. Zhang, Z. Sun, F. Chen, Z. Ye, M. Xu, Q. Ge, S. Tan, X. Niu, M. Xia, B. Xie, Y. Li, X. Chen, H. Wen, and D. Feng, Nature Communications **4**, 3010 (2013).
[7] K. Chen, T.-C. Weng, G. Schmerber, V. N. Gurin, J.-P. Kappler, Q. Kong, F. Baudelet, A. Polian, and L. Nataf, Physical Review B **97**, 235153 (2018).
[8] W. T. Fuhrman, J. C. Leiner, J. W. Freeland, M. van Veenendaal, S. M. Koohpayeh, W. A. Phelan, T. M. McQueen, and C. Broholm, Physical Review B **99**, 020401 (2019).
[9] Y. Li, Q. Ma, S. X. Huang, and C. L. Chien, Science Advances **4**, 10.1126/sciadv.aap8294 (2018).
[10] Y. S. Eo, A. Rakoski, J. Lucien, D. Mihaliov, Çağlıyan Kurdak, P. F. S. Rosa, and Z. Fisk, Proceedings of the National Academy of Sciences **116**, 12638 (2019).
[11] S. Gabáni, E. Bauer, S. Berger, K. Flachbart, Y. Paderno, C. Paul, V. Pavlík, and N. Shitsevalova, Physical Review B **67**, 172406 (2003).
[12] N. Harrison, Physical Review Letters **121**, 026602 (2018).
[13] Y. Zhou, P. F. S. Rosa, J. Guo, S. Cai, R. Yu, S. Jiang, K. Yang, A. Li, Q. Si, Q. Wu, Z. Fisk, and L. Sun, Physical Review B **101**, 125116 (2020).
[14] T. Takimoto, Journal of the Physical Society of Japan **80**, 123710 (2011).
[15] P. F. Rosa and Z. Fisk, arXiv preprint arXiv:2007.09137 (2020).

[16] S. Süllow, I. Prasad, M. C. Aronson, J. L. Sarrao, Z. Fisk, D. Hristova, A. H. Lacerda, M. F. Hundley, A. Vigliante, and D. Gibbs, Physical Review B **57**, 5860 (1998).
[17] S. Süllow, I. Prasad, M. C. Aronson, S. Bogdanovich, J. L. Sarrao, and Z. Fisk, Physical Review B **62**, 11626 (2000).
[18] W. Henggeler, H.-R. Ott, D. Young, and Z. Fisk, Solid State Communications **108**, 929 (1998).
[19] M. Pohlit, S. Rößler, Y. Ohno, H. Ohno, S. von Molnár, Z. Fisk, J. Müller, and S. Wirth, Physical Review Letters **120**, 257201 (2018).
[20] D. J. Sivananda, A. Kumar, M. A. Ali, S. S. Banerjee, P. Das, J. Müller, and Z. Fisk, Physical Review Materials **2**, 113404 (2018).
[21] P. Nyhus, S. Yoon, M. Kauffman, S. L. Cooper, Z. Fisk, and J. Sarrao, Physical Review B **56**, 2717 (1997).
[22] R. S. Manna, P. Das, M. de Souza, F. Schnelle, M. Lang, J. Müller, S. von Molnár, and Z. Fisk, Physical Review Letters **113**, 067202 (2014).
[23] M. A. Anisimov, A. V. Bogach, A. V. Kuznetsov, A. N. Azarevich, N. A. Samarin, S. V. Demishev, N. Y. Shitsevalova, A. V. Dukhnenko, V. B. Filipov, N. E. Sluchanko, and V. V. Glushkov, Physics of the Solid State **61**, 565 (2019).
[24] S. Nie, Y. Sun, F. B. Prinz, Z. Wang, H. Weng, Z. Fang, and X. Dai, Physical Review Letters **124**, 076403 (2020).
[25] Y. Takahashi, M. Fujimoto, M. Tsuchiko, and K.-I. Ohshima, Journal of Applied Crystallography **34**, 208 (2001).
[26] J. Duan, T. Zhou, L. Zhang, J.-G. Du, G. Jiang, and H.-B. Wang, Chinese Physics B **24**, 096201 (2015).
[27] J. C. Cooley, M. C. Aronson, J. L. Sarrao, and Z. Fisk, Physical Review B **56**, 14541 (1997).
[28] R. G. Goodrich, N. Harrison, J. J. Vuillemin, A. Teklu, D. W. Hall, Z. Fisk, D. Young, and J. Sarrao, Physical Review B **58**, 14896 (1998).
[29] J. D. Denlinger, G.-H. Gweon, S.-K. Mo, J. W. Allen, J. L. Sarrao, A. D. Bianchi, and Z. Fisk, Journal of the Physical Society of Japan **71**, 1 (2002).
[30] M. Kasaya, J. Tarascon, J. Etourneau, and P. Hagenmuller, Materials Research Bulletin **13**, 751 (1978).
[31] J. Kuneš and W. E. Pickett, Physical Review B **69**, 165111 (2004).
[32] N. Foroozani, J. Lim, G. Fabbris, P. Rosa, Z. Fisk, and J. Schilling, Physica B: Condensed Matter **457**, 12 (2015).
[33] Z. Fisk, D. C. Johnston, B. Cornut, S. von Molnar, S. Oseroff, and R. Calvo, Journal of Applied Physics **50**, 1911 (1979).
[34] W. A. Phelan, S. M. Koohpayeh, P. Cottingham, J. A. Tutmaher, J. C. Leiner, M. D. Lumsden, C. M. Lavelle, X. P. Wang, C. Hoffmann, M. A. Siegler, N. Haldolaarachchige, D. P. Young, and T. M. McQueen, Scientific Reports **6**, 20860 (2016).
[35] Y. S. Eo, A. Rakoski, J. Lucien, D. Mihaliov, Ç. Kurdak, P. F. Rosa, and Z. Fisk, Proceedings of the National Academy of Sciences **116**, 12638 (2019).
[36] P. F. S. Rosa and Z. Fisk, Flux methods for growth of intermetallic single crystals (2018).
[37] D. Haskel, Y. C. Tseng, N. M. Souza-Neto, J. C. Lang, S. Sinogeikin, Y. Mudryk, K. A. Gschneidner, and V. K. Pecharsky, High Pressure Research **28**, 185 (2008).
[38] R. Hrubiak, S. Sinogeikin, E. Rod, and G. Shen, Review of Scientific Instruments **86**, 072202 (2015).
[39] G. Shen, Y. Wang, A. Dewaele, C. Wu, D. E. Fratanduono, J. Eggert, S. Klotz, K. F. Dziubek, P. Loubeyre, O. V. Fat'yanov, P. D. Asimow, T. Mashimo, and R. M. M. Wentzcovitch, High Pressure Research **40**, 299 (2020).
[40] C. Prescher and V. B. Prakapenka, High Pressure Research **35**, 223 (2015).
[41] "See Supplemental Material at [url] for extra details and datasets.
[42] J. Y. Zhao, W. Bi, S. Sinogeikin, M. Y. Hu, E. E. Alp, X. C. Wang, C. Q. Jin, and J. F. Lin, Review of Scientific Instruments **88**, 125109 (2017).
[43] O. Bunău and Y. Joly, Journal of Physics: Condensed Matter **21**, 345501 (2009).
[44] N. M. Souza-Neto, J. Zhao, E. E. Alp, G. Shen, S. V. Sinogeikin, G. Lapertot, and D. Haskel, Physical Review Letters **109**, 026403 (2012).
[45] R. dos Reis, L. Veiga, G. Fabbris, F. Garcia, D. Haskel, F. Gandra, and N. Souza-Neto, Journal of Magnetism and Magnetic Materials **560**, 169619 (2022).
[46] W. Bi, N. M. Souza-Neto, D. Haskel, G. Fabbris, E. E. Alp, J. Zhao, R. G. Hennig, M. M. Abd-Elmeguid, Y. Meng, R. W. McCallum, K. Dennis, and J. S. Schilling, Physical Review B **85**, 205134 (2012).
[47] H. Martinho, C. Rettori, G. M. Dalpian, J. L. Da Silva, Z. Fisk, and S. B. Oseroff, Journal of Physics Condensed Matter **21**, 10.1088/0953-8984/21/45/456007 (2009).
[48] B. H. Toby and R. B. V. Dreele, Journal of Applied Crystallography **46**, 544 (2013).
[49] R. Sereika, M. P. Clay, L. Zhu, P. F. S. Rosa, W. Bi, and Y. K. Vohra, Journal of Applied Physics **134**, 10.1063/5.0173376 (2023).
[50] F. Grandjean and G. J. Long, Mössbauer spectroscopy of europium-containing compounds (1989).
[51] W. Bi, J. Lim, G. Fabbris, J. Zhao, D. Haskel, E. E. Alp, M. Y. Hu, P. Chow, Y. Xiao, W. Xu, and J. S. Schilling, Physical Review B **93**, 184424 (2016).
[52] W. Sturhahn, Hyperfine Interactions **125**, 149 (2000).

[53] J. M. Coey, O. Massenet, M. Kasaya, and J. Etourneau, Le Journal de Physique Colloques **40**, C2 (1979).
[54] S. A. Shaheen, M. Abd-Elmeguid, H. Micklitz, J. S. Schilling, P. Klavins, and R. N. Shelton, Physical Review Letters **55**, 312 (1985).
[55] S. K. Malik, G. K. Shenoy, S. M. Heald, and J. M. Tranquada, Physical Review Letters **55**, 316 (1985).
[56] Z. Nix, J. Zhao, E. E. Alp, Y. Xiao, D. Zhang, G.-H. Cao, Y. K. Vohra, and W. Bi, Journal of Physics: Condensed Matter **34**, 415601 (2022).
[57] Y. Ōnuki, A. Nakamura, F. Honda, D. Aoki, T. Tekeuchi, M. Nakashima, Y. Amako, H. Harima, K. Matsubayashi, Y. Uwatoko, S. Kayama, T. Kagayama, K. Shimizu, S. Esakki Muthu, D. Braithwaite, B. Salce, H. Shiba, T. Yara, Y. Ashitomi, H. Akamine, K. Tomori, M. Hedo, and T. Nakama, Philosophical Magazine **97**, 3399 (2017).
[58] W. Bi, J. Lim, G. Fabbris, J. Zhao, D. Haskel, E. E. Alp, M. Y. Hu, P. Chow, Y. Xiao, W. Xu, and J. S. Schilling, Phys. Rev. B **93**, 184424 (2016).
[59] D. Haskel, E. A. Stern, and H. Shechter, Phys. Rev. B **57**, 8034 (1998).
[60] P. Blaha, K. Schwarz, F. Tran, R. Laskowski, G. K. H. Madsen, and L. D. Marks, The Journal of Chemical Physics **152**, 074101 (2020).
[61] G. Loula, R. dos Reis, D. Haskel, F. Garcia, N. Souza-Neto, and F. Gandra, Physical Review B **85**, 245128 (2012).
[62] D. Sheets, V. Flynn, J. Kim, M. Upton, D. Casa, T. Gog, Z. Fisk, M. Dzero, P. F. Rosa, D. G. Mazzone, *et al.*, Journal of Physics: Condensed Matter **32**, 135601 (2019).
[63] M. Peters, K. Kliemt, M. Ocker, B. Wolf, P. Puphal, M. Le Tacon, M. Merz, M. Lang, and C. Krellner, Physical Review Materials **7**, 064405 (2023).
[64] Y. Ōnuki, M. Hedo, and F. Honda, journal of the physical society of japan **89**, 102001 (2020).
[65] A. Mitsuda, S. Hamano, N. Araoka, H. Yayama, and H. Wada, Journal of the Physical Society of Japan **81**, 023709 (2012).
[66] A. Nakamura, T. Nakama, K. Uchima, N. Arakaki, C. Zukeran, S. Komesu, M. Takeda, Y. Takaesu, D. Nakamura, M. Hedo, K. Yagasaki, and Y. Uwatoko, Journal of Physics: Conference Series **400**, 032106 (2012).
[67] G. Dionicio, H. Wilhelm, Z. Hossain, and C. Geibel, Physica B: Condensed Matter **378-380**, 724 (2006).
[68] P. Proschek, J. Prchal, M. Diviš, J. Prokleška, K. Vlášková, J. Valenta, J. Zubáč, J. Kaštil, M. Hedo, T. Nakama, *et al.*, Journal of Alloys and Compounds **864**, 158753 (2021).
[69] S. Nie, Y. Sun, F. B. Prinz, Z. Wang, H. Weng, Z. Fang, and X. Dai, Physical Review Letters **124**, 076403 (2020).

Supplementary materials

I. X-RAY DIFFRACTION

In order to obtain the powder diffraction patterns for EuB_6 the DAC was placed at 287.8 mm distance from the marCCD mosaic 220. The X-ray at EMA beamline was set to 0.4859 Å wavelength. Using the DIOPTAS software a mask was applied to spots where diffracted beams saturated the CCD as shown in Figure S1 (b). Then, with appropriate calibration obtained with a LaB_6 pattern previously measured, the pattern was integrated utilizing an azimuth angle in an interval such that all diffraction lines were fully visible inside the CCD. This procedure was repeated for every pressure point in order to obtain the integrated diffraction patterns shown in Figure S2. We notice that at 11.86 and 13.48 degrees we observe peaks that are coming from a portion of the X-ray diffracting in the Rhenium gasket utilized for the experiment. In Figure S1 it is possible to observe that at these 2θ angles there is a constant weak haze which clearly differs from the several other peaks coming from the sample. Another indication that these peaks are coming from the gasket is the fact that they do not follow any trend with increasing pressure as any other peaks coming from EuB_6.

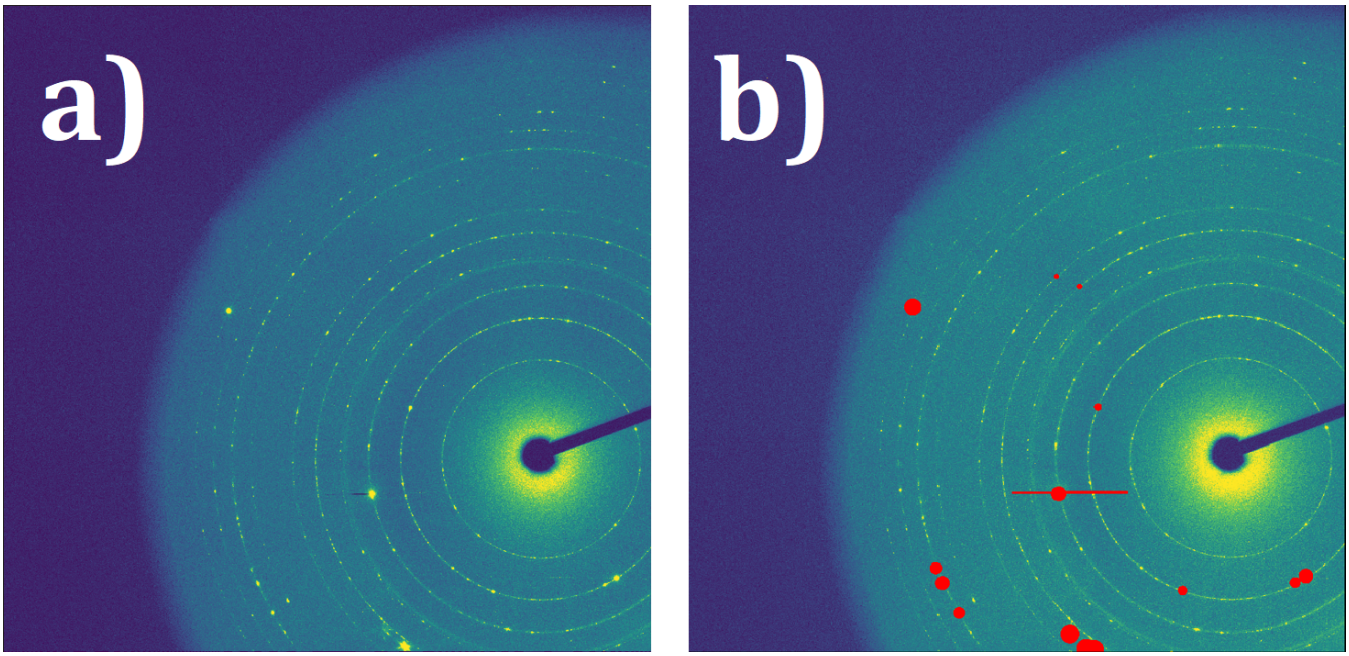

Fig. S1: a) Powder diffraction pattern obtained at 10.8 GPa pressure. b) The same diffraction pattern masked (red spots) in order to avoid integrating saturated pixels

.

With GSAS-II software[1] the integrated patterns were then refined utilizing Le-bail refinement together with a initial crystallographic (.cif)[2] file to identify the peaks for the EuB_6 cubic phase. The instrumental parameter was set as a Debye-Sccherrer type with distance between sample and CCD used as goniometer radius. Background radiation was fit using a third order Chebyschev-1 function. The refinement regions range were set to be for a 2θ starting at 5.3 degrees up to 18 degrees. For each pressure step the lattice parameter was set to be fitted in order to obtain the unit cell volume. The starting volume for each pressure was set to be the one found in the preceding pressure point, except for 1.5 GPa were the standard ambient pressure volume was used as a starting parameter.

The result for unit cell volume in function of applied pressure was summarized in the graph shown in the main text, Figure 2, where we also utilized the Birch-Murnagham equation of state to fit the observed compression behavior.

II. XANES MEAN VALENCE ESTIMATE

In order to estimate the mean valence shift for Eu in the compound, simulations utilizing the FDMNES software package for XANES spectra were performed. To fit the experimental data, trial and error simulations were performed

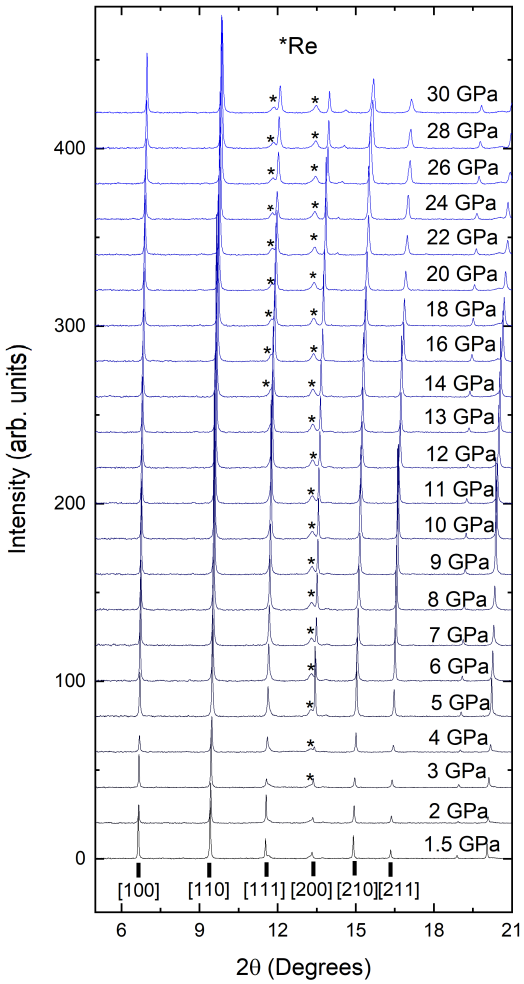

Fig. S2: Integrated diffraction patterns for all measured pressure points at ambient temperature. Peaks are marked to each corresponding crystallographic direction, broadened peaks marked with stars are arising from the rhenium gasket.

where Eu^{3+} absorption spectra was dislocated 8 eV above Eu^{2+} to match experimental data. Several parameters were tweaked such as Gamma hole lifetime and Gaussian width in order to fit the absorption peaks Lorentzian profiles. Then, the ab-initio absorption peaks were obtained for each relevant pressure by adjusting the lattice parameter following the Birch-Murnaghan EOS. This approach helps to account for any absorption peak change due to lattice contraction, although it is still possible that the 3+ population is being overestimated. Finally, a weighted addition of both Eu^{2+} and Eu^{3+} was performed in order to obtain curves and estimate the mean Eu valence, uncertainty was estimated by inspection of peaks with of peaks with $\pm 2\%$ ion population. Figure S3 shows XANES experimental data for 2.5 GPa and 28.5 GPa to highlight the difference between absorption spectra. The inset shows the FDMNES simulated absorption peaks for 28.5 GPa. Figure S4 show all the experimental simulated curves utilized to obtain the mean valence and its uncertainty of Eu in the compound.

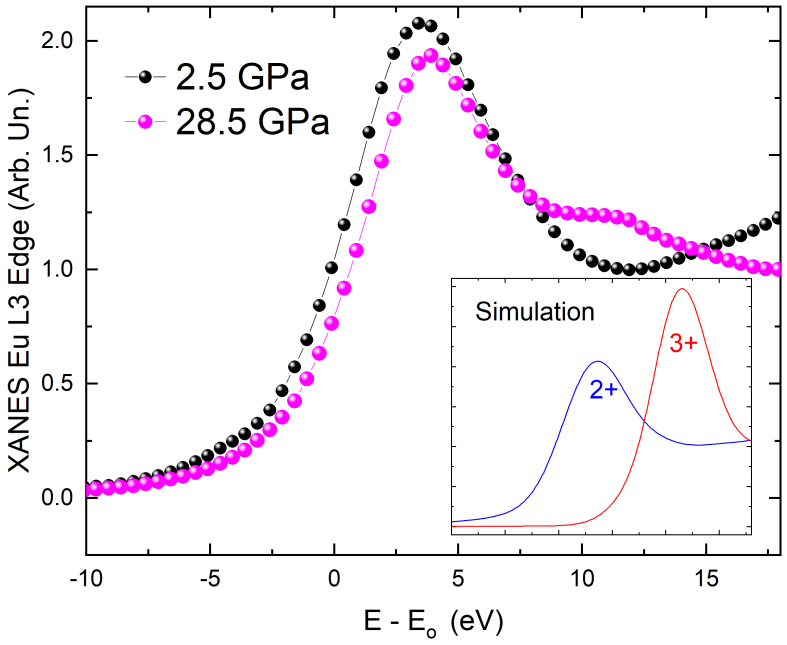

Fig. S3: Normalized Eu L_3 x-ray absorption data at two selected pressures. The inset shows theoretical absorption spectra for Eu^{2+} and Eu^{3+} at 28.5 GPa.

III. XMCD SUPPLEMENTARY DATA

The XMCD signal of the sample at ambient pressure was measured in several different temperatures. The results for selected temperatures can be seen in Figure S5. It is possible to observe the evolution of the XMCD signal as temperature increases. Most interestingly is that at 25 K, which is above both T_{c1} and T_{c2}, there is still a XMCD signal present. The origins of such magnetic signal can be related to the presence of magnetic polarons in the sample which were previously shown to start forming around 40 K of temperature via STM experiments[3]. In Figure S6 we present data for XMCD performed in a membrane with EuB_6 powder obtained by crushing single crystals from the same batch as the high pressure experiments. We see a very well defined signal typical for ferromagnetic materials at 6 K while at 25 K we see a linear increase for the XMCD signal in function of field since the sample is at a paramagnetic state at this temperature at ambient pressure. In Figure S7 we see SQUID measurements for EuB_6 that shows a similar behavior observed with XMCD signal. High pressure measurements for magnetic field dependence of the XMCD signal were also performed ranging from -20 kOe up to 20 kOe for several pressures at 6 K in order to better determine the magnetic behavior of the sample in such conditions. The results for selected pressures can be seen in Figure S8 where at ambient pressure, 2.5 GPa and 10 GPa we clearly see a pattern associated to a ferromagnet under magnetic fields resembling a hysteresis loop with low coercivity as is the case for EuB_6. For 20 GPa and 28 GPa the signal remains at noise level for all applied magnetic field. We observed a significant difference in the ratio of paramagnetic and ordered state magnetization signals between the low-pressure ordered state and the high-pressure state, which supports the idea that the XMCD signal observed above 20 GPa is a result of an AFM ordered state.

IV. DFT CALCULATIONS

Density Function Theory (DFT) were made utilizing the Wien2K[4,5] package via muffin-tin method for Kohn-Sham solutions in which wave-functions are written as a combination of spherical harmonics and radial functions in a spacial region at a distance from the nuclei inferior to a RMT radius and plane waves for regions further than RMT[5]. The DFT+U method[6] with generalized gradient approximation[7] was employed for our simulations.

In the cubic *Pm*-3*m* EuB_6 structure the Eu atoms are at the unit cell vertices while the boron atoms are arranged

in a octahedral pattern at unit cell's center. It is important to notice that the boron octahedra may vary in size while conserving crystalline symmetry. Therefore there is a free parameter δu which is the distance between a boron atom and its closest Eu defined cubic face. This coordinate is given as a fraction of the lattice parameter and may vary as the cell is compressed or expanded. For these simulations theoretical values for the unit cell following the Birch-Murnagham equation of state were utilized in order to simulate pressure being applied in the compound.

Our simulations accounted for spin polarization, the separation between core and valence orbitals were made utilizing an energy of -6 Ry. For Eu, this energy resulted in core levels: 1s 2s 2p 3s 3p 3d 4s 4p 4d with energies <-9.5 Ry, and valence states 5s 5p 4f 5d 6s with energies > -3.0 Ry. For the boron atom the 1s orbital was considered as a core level with energy <-13.2 Ry (≈ -13.27 for spin up and ≈ -13.25 for spin down) the 2s and 2p orbitals were considered as valence levels with energies > -0.8 Ry. The first Brillouin zone sampling was performed in a 20x20x20 K-points lattice and the plane waves number utilized was defined by the internal parameter $R_{MT}K_{max} = 7$ for the wave-functions and $G_{max} = 12$ for electronic density. The DFT+U method was applied for Eu-f orbitals utilizing U = 7 eV[8].

The unit cell was simulated with different levels of compression in order to obtain its electronic and magnetic structures in several different applied pressures. The unit cell volume was varied between 80 % and 110 % with respect to the ambient pressure value $V_0 = (4.185^3$ Å^3 $)$[9] while maintaining crystalline symmetry. As for to refine boron atoms position (δu) an optimization for atomic coordinates was performed concomitant to the self-consistent cycle for Kohn-Sham equations DFT calculus[5]. The initial utilized value was of $\delta u_0 = 0.203$ and after atomic position optimization the total forces over boron atoms were less than 2x10^{-4} mRy/Bohr. Figure S9 a) shows the optimized δu value as function of unit cell compression (V/V_0). This procedure guarantees that the utilized structure for each pressure point is at its local minimum energy level.

In order to certify that calculated structure matched experimental observations the first analysis was to determine a theoretical equation of state adjusting energy levels for unit cell compression as shown in S9 b) into the Birch-Murnaghan EOS. This fit gave us $B_o = 153(1)$ GPa and $B_o^{'} = 3.3(1)$ which only varies slightly from previous theoretical values found by Duan et al[10] ($B_o = 152.4$ GPa and $B_o^{'} = 3.59$) and is close to our reported parameters found fitting experimental data. A plot for the theoretical obtained EOS can be found in Figure S9 c) and it was utilized to associate values of unit cell compression to applied pressures.

Figure S10 shows obtained results for occupation (in e$^-$ units) and magnetic moments (in μ_B) for Eu and B atoms, interstitial space and for each Eu orbital as well. Figure S10 a) shows the total charge inside the muffin-tin spheres for Eu and B atoms as well as for interstitial region. The most significant variation was observed in the interstice (+4.04 %), accompanied by lesser variations in boron (-2.99 %) and Europium (0.252 %). The charge balance results in a liquid charge transfer in which the boron atoms (muffin-tin spheres, $r < R_{MT}$) lose electrons in favor of Eu and interstitial space. Even though Eu present a lesser percentage change in comparison to boron the analysis for partial charges evolution in function of pressure, shown in Figure S10 b), reveals a considerable increase of 74.3 % in 5d orbital occupation. This increase was accompanied by variations of less than 1% in the remaining orbitals (0.868 % for 5s+6s, 0.761 % for 5p and -0.909 % for 4f), in such way that the variation in the 5d orbital is the main responsible for the charge increase in the Eu atom.

As discussed in the main text, our DFT simulations show a shift in Eu 4f electronic occupations towards 5d occupation, this may be related to a shift of Eu^{2+} towards Eu^{3+} which would be in quantitative agreement with the observed mean valence increase estimated with XANES measurements. Another relevant result observed in our simulations is the increase of interstitial net charge which may point towards a scenario where this charge transfer contributes to the increase of a quadrupolar interaction which would explain a paramagnetic state as proposed in one of our interpretations for the Synchrotron Mösssbauer Spectroscopy data.

V. SMS SUPPLEMENTARY DATA

As discussed in the main text, paramagnetic behavior above 20 GPa cannot be completely ruled out. Therefore we here present in Figures S11 and S12 experimental curves and fits for a model where paramagnetic behavior occurs at 21 GPa and above at T = 20 K and T = 9 K respectively. It is clear that the model provides satisfactory fits for both temperatures, in the pressure range where the new magnetic state is observed.

In order to explain the quantum beats appearing above 21 GPa in the SMS data for the model with a paramagnetic state we propose the appearing of a giant quadrupole splitting signal. Such QI was previously reported fo Eu based compounds before[11,12] and one of the hypotheses raised to explain such great QI signal was that Eu is in the verge of valence instability. The caveat for such scenario is that EuB_6 presents a cubic symmetry with Eu with a $\overline{3}m$ point symmetry. In Table I we show the χ^2 obtained via CONUSS software for our fits for 24 GPa and 29.5 GPa. Although the PM state present a better fit with lesser value of χ^2 it is still challenging to physically justify such a great QI in EuB_6 that arises in this model. Regardless of that, our DFT calculation shows a decrease in charge in Eu inner

TABLE I: Table showing the values of χ^2 for 24 GPa and 29.5 GPa for AFM and PM CONUSS software fits.

AFM P (GPa)	9 K χ^2	20 K χ^2
24	27	6.87
29.5	26	12.75
PM P (GPa)	9 K χ^2	20 K χ^2
24	17.04	5.11
29.5	20.03	5.94

shells and B atoms and a increase in Eu outer shells and interstitial state. As discussed above this could indicate an increase in band overlap and a greater hybridization of states for the Eu atom. This is in agreement with our XANES data which shows a shift in Eu mean valence from 2+ towards 3+. In addition, there is no temperature dependence in between SMS signals collected at 9 K and 20 K. This is clearly shown in Figure S13 where both SMS data for 29.5 GPa at these temperature overlap almost in the entire measured range. Therefore it is possible to interpret such data as showing no magnetic transition between this two temperatures, which can indicate that the sample is either antiferromagnetic or paramagnetic in this entire temperature range (between 9 K and 20 K). In Figure S15 we present the equivalent of conventional Mösssbauer of the SMS models for a broader comparison purpose.

[1] B. H. Toby and R. B. V. Dreele, Journal of Applied Crystallography **46**, 544 (2013), ISSN 0021-8898.
[2] J. Tarascon, J. Soubeyroux, J. Etourneau, R. Georges, J. Coey, and O. Massenet, Solid State Communications **37**, 133 (1981).
[3] M. Pohlit, S. Rößler, Y. Ohno, H. Ohno, S. von Molnár, Z. Fisk, J. Müller, and S. Wirth, Physical Review Letters **120**, 257201 (2018), ISSN 0031-9007.
[4] P. Blaha, K. Schwarz, G. Madsen, D. Kvasnicka, J. Luitz, and K. Schwarz, *An augmented planewave+ local orbitals program for calculating crystal properties revised edition wien2k 13.1 (release 06/26/2013) wien2k users guide* (2013).
[5] P. Blaha, K. Schwarz, F. Tran, R. Laskowski, G. K. H. Madsen, and L. D. Marks, The Journal of Chemical Physics **152**, 074101 (2020), ISSN 0021-9606.
[6] S. A. Tolba, K. M. Gameel, B. A. Ali, H. A. Almossalami, and N. K. Allam, Density Functional Calculations-Recent Progresses of Theory and Application **1**, 5772 (2018).
[7] J. P. Perdew, K. Burke, and M. Ernzerhof, Physical review letters **78**, 1396 (1997).
[8] J. Kuneš and W. E. Pickett, Physical Review B **69**, 165111 (2004), ISSN 1098-0121.
[9] M. Blomberg, M. Merisalo, M. Korsukova, and V. Gurin, Journal of alloys and compounds **217**, 123 (1995).
[10] J. Duan, T. Zhou, L. Zhang, J.-G. Du, G. Jiang, and H.-B. Wang, Chinese Physics B **24**, 096201 (2015).
[11] S. A. Shaheen, M. Abd-Elmeguid, H. Micklitz, J. S. Schilling, P. Klavins, and R. N. Shelton, Physical Review Letters **55**, 312 (1985), ISSN 0031-9007.
[12] S. K. Malik, G. K. Shenoy, S. M. Heald, and J. M. Tranquada, Physical Review Letters **55**, 316 (1985), ISSN 0031-9007.

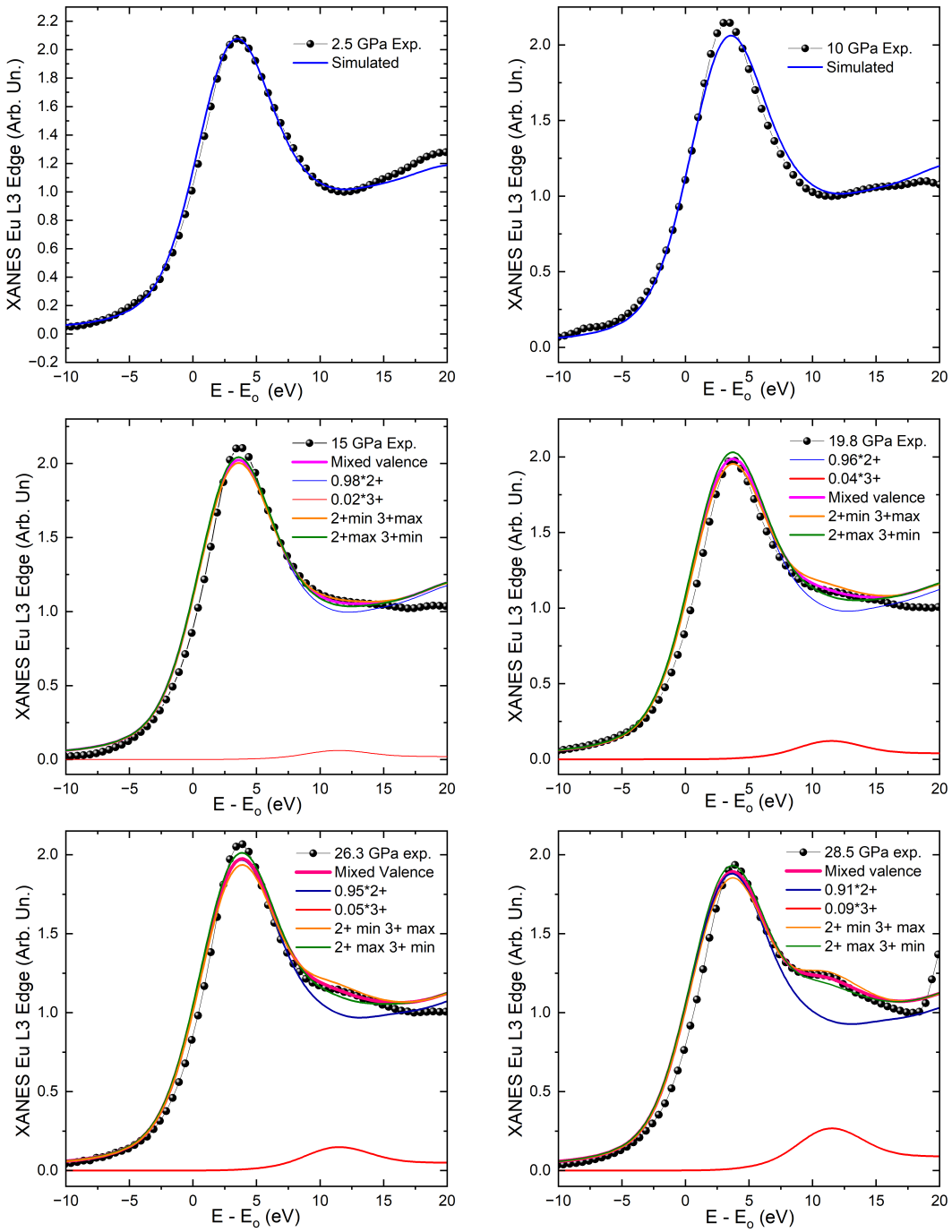

Fig. S4: XANES Eu L_3 edge experimental data (black points) and simulated data (solid lines) for several pressures indicated in the graphs. There is no linear combination for 2.5 GPa and 10 GPa since there is no discernible Eu^{3+} peak. The mixed valence curve (magenta) are the result from the weighted sum of 2+ and 3+ (blue and red, respectively) Eu ions absorption. Uncertainty was determined by tracking maximum and minimum value curves (orange and green), corresponding to a range of plus or minus 0.02 in the reported values (equivalent to ±2% in ion population). The total sum of the weighted additions always equals to 1.

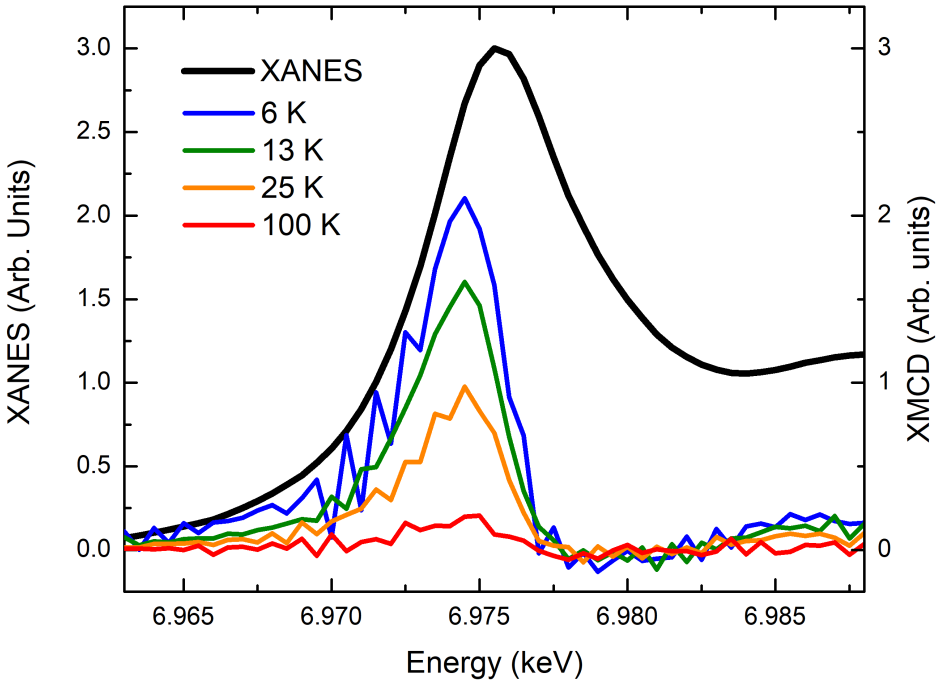

Fig. S5: Ambient pressure measurements for XANES (left vertical axis) and XMCD signal (right vertical axis) for 6 K, 13 K, 25 K and 100 K. It is possible to see a XMCD signal up to 25 K, but signal nearly vanishes at 100 K.

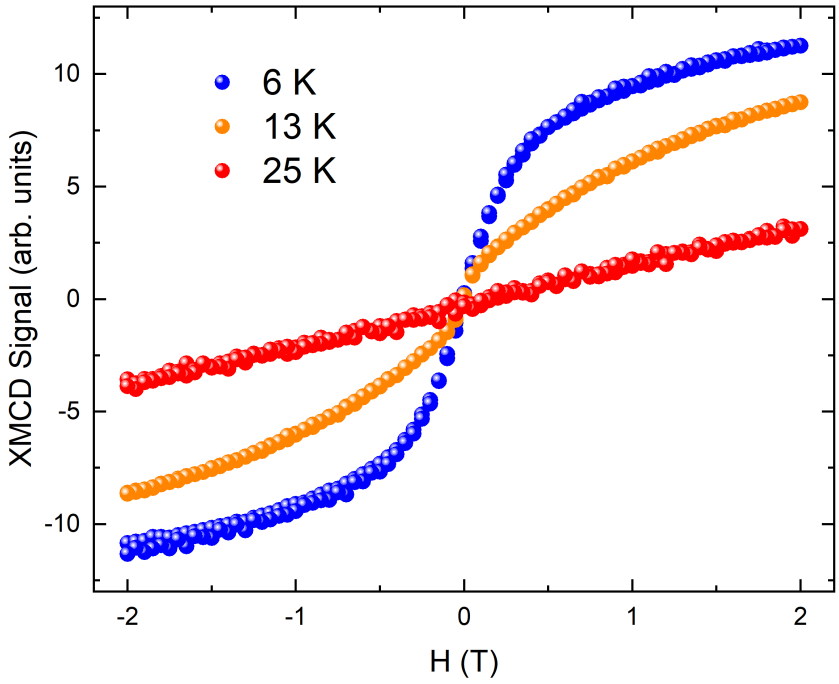

Fig. S6: Ambient pressure measurements XMCD signal for 6 K, 13 K and 25 K as a function of applied magnetic field.

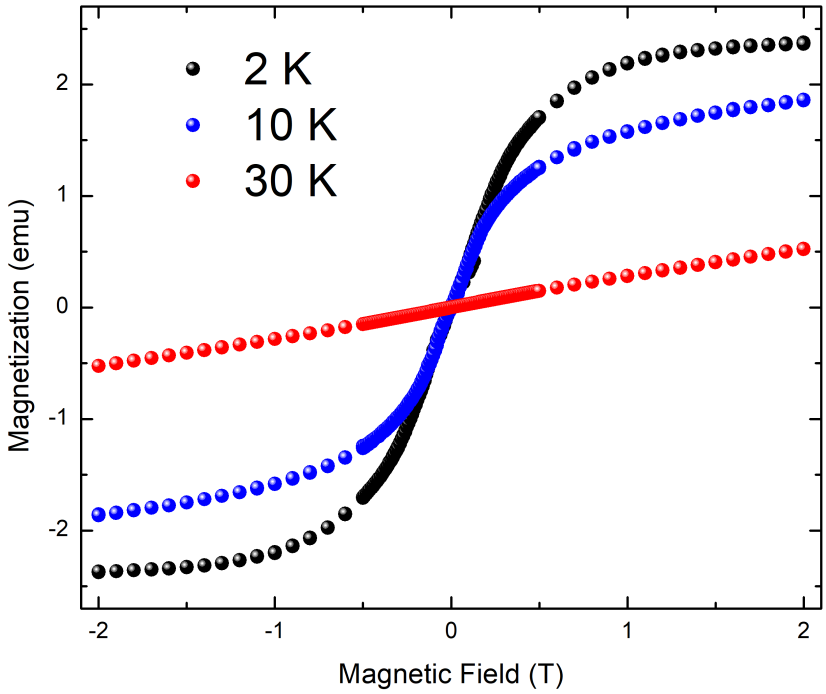

Fig. S7: Ambient pressure measurements for magnetization as a function of applied field.

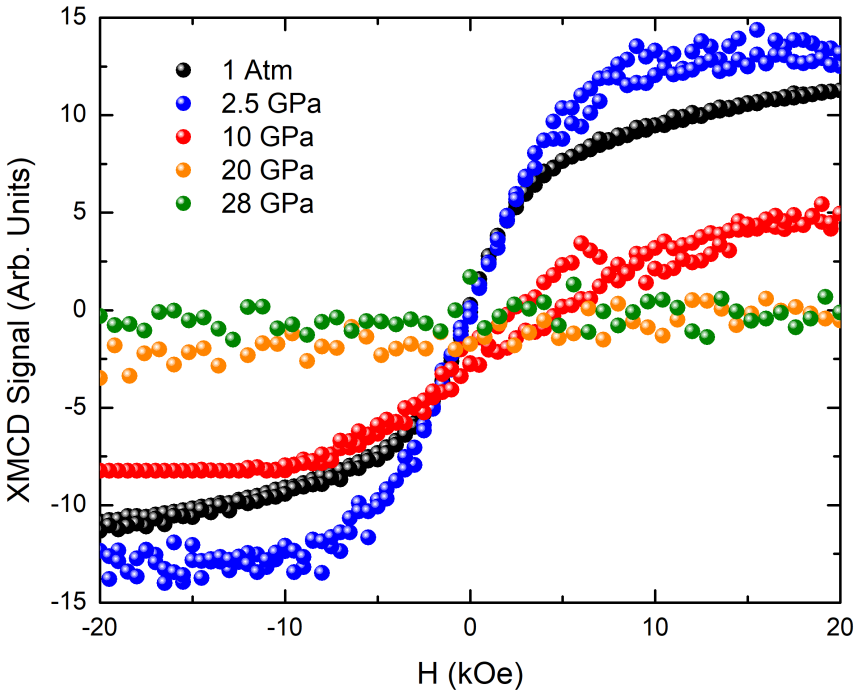

Fig. S8: XMCD signal for selected pressures at 6 K as a function of magnetic field. It is possible to see that at 1 atm (ambient pressure), 2.5 GPa and 10 GPa we see an hysteresis-like loop shape as expected for ferromagnetic materials. At 20 GPa and 28 GPa the signal is at noise level demonstrating that the ferromagnetism was fully suppressed.

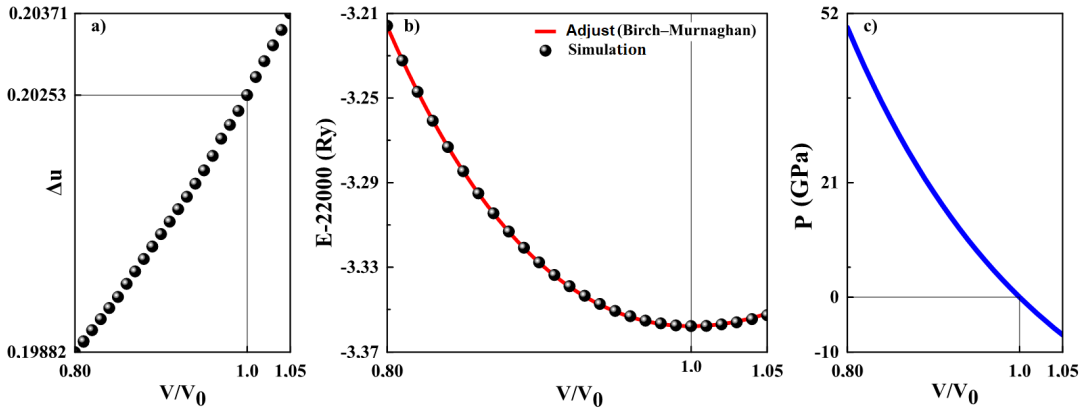

Fig. S9: Structural and energetic analysis for EuB_6 unit cell compression values (V/V_0) between 0.80 and 1.05. a) Internal parameter δu in lattice parameter units. b) Unit cell energy for different compression with adjusted fits using Birch-Murnagham equation of state. c) Adjusted Birch-Murnaghan equation of state.

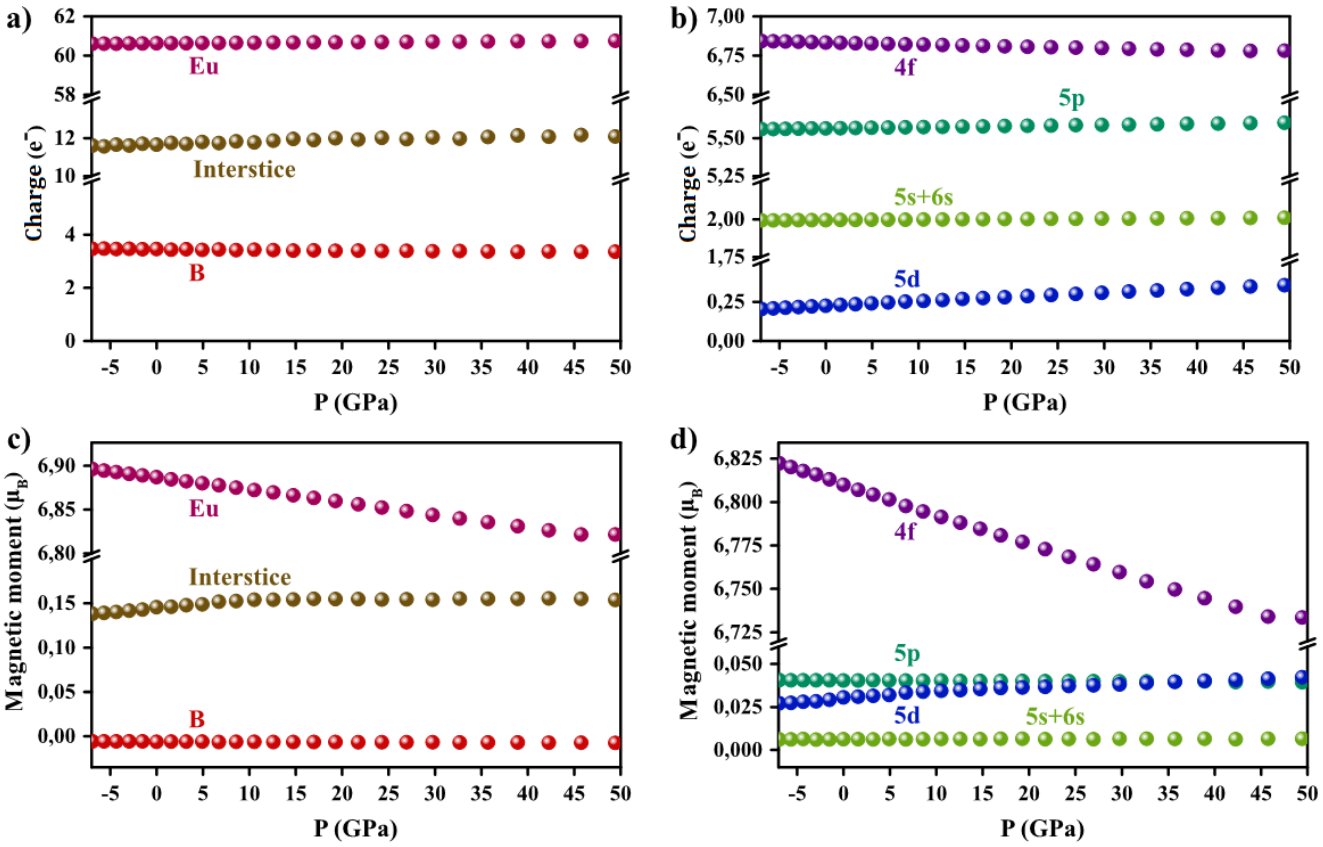

Fig. S10: DFT results for EuB_6 electronic occupations and magnetic moments under pressure. a) Total charge for Eu and B atoms and in the interstitial region. b) Eu atom orbital occupations. c) Eu, B and interstice contribution for the compound's magnetism. d) Magnetic moment for selected Eu orbitals.

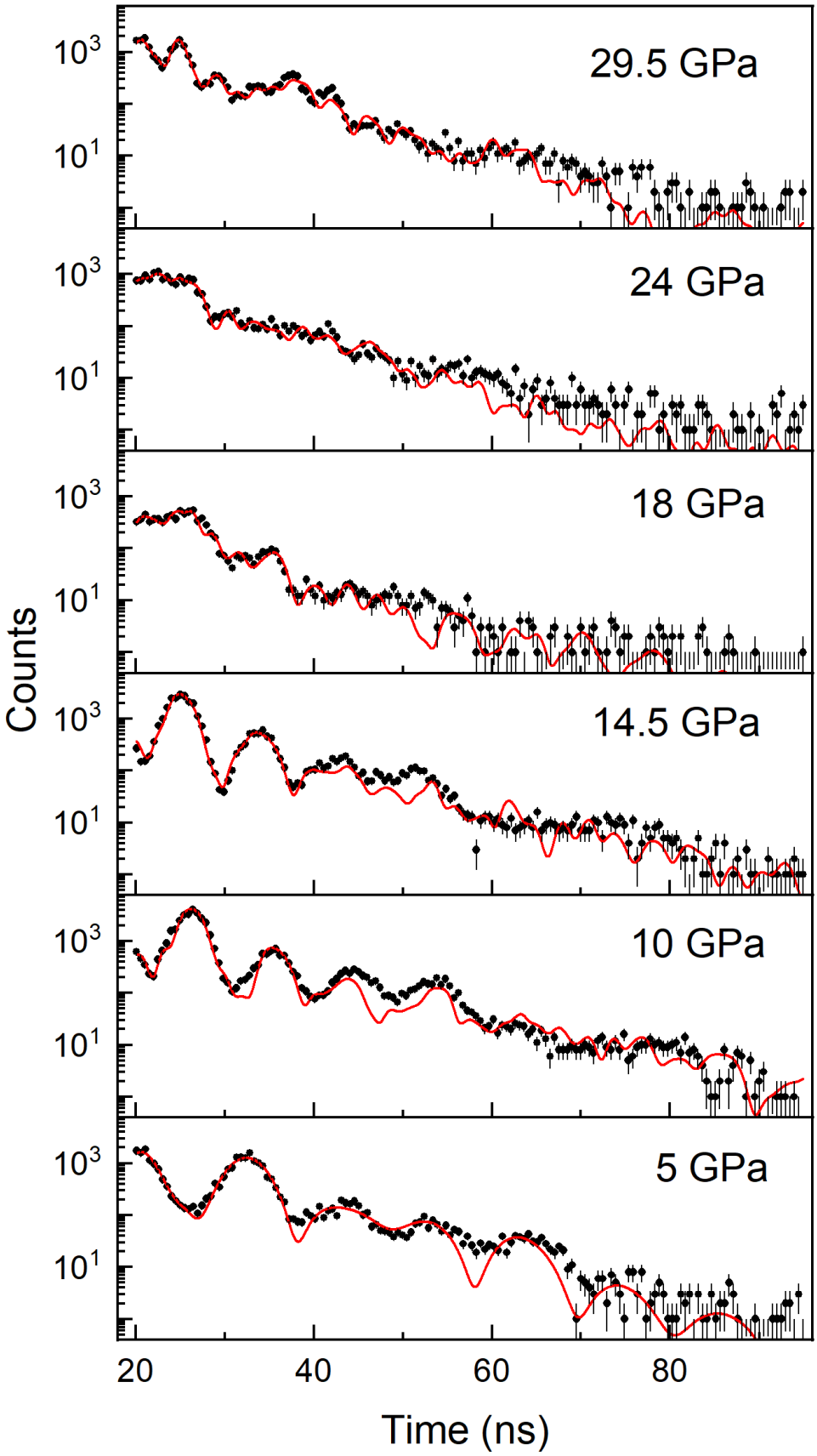

Fig. S11: Fits of SMS data at T=20 K assuming paramagnetic interactions above 20 GPa, and ferromagnetic behavior below 18 GPa.

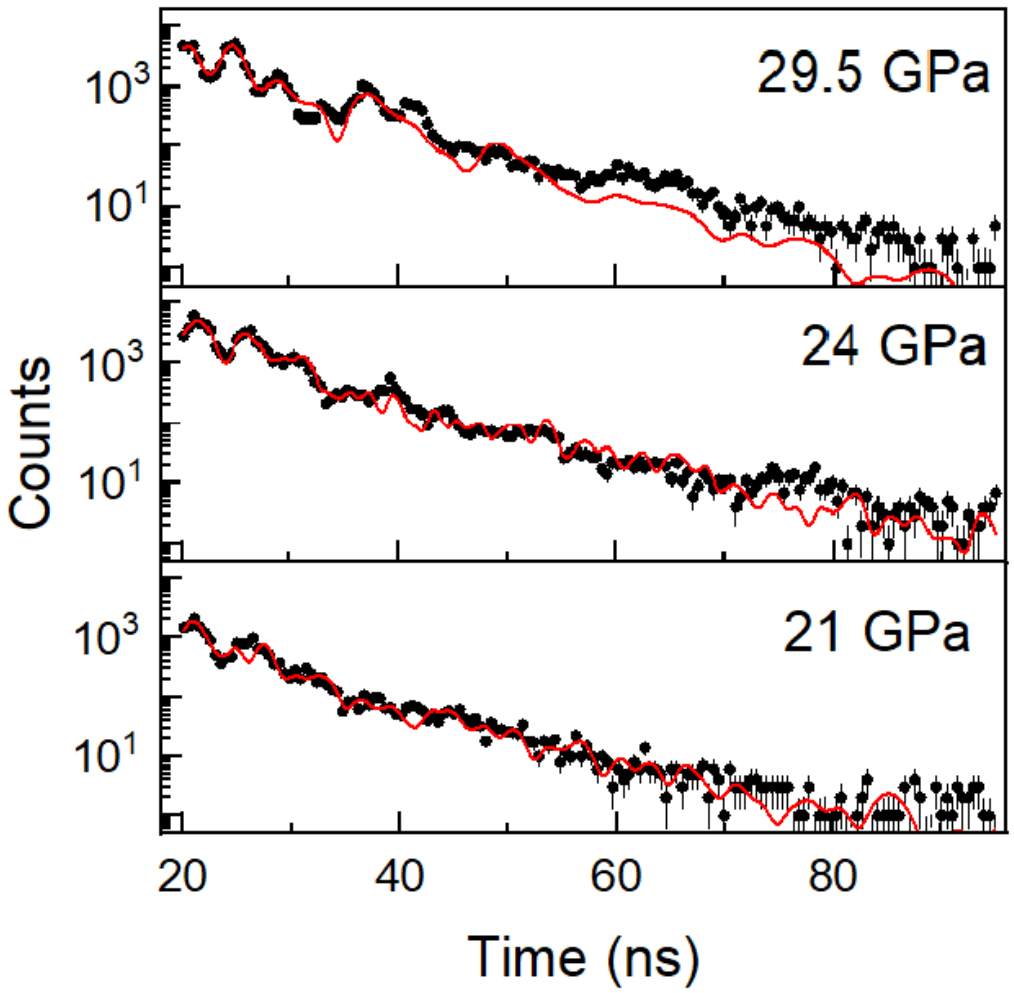

Fig. S12: Fits of SMS data at T=9 K assuming paramagnetic interactions above 20 GPa

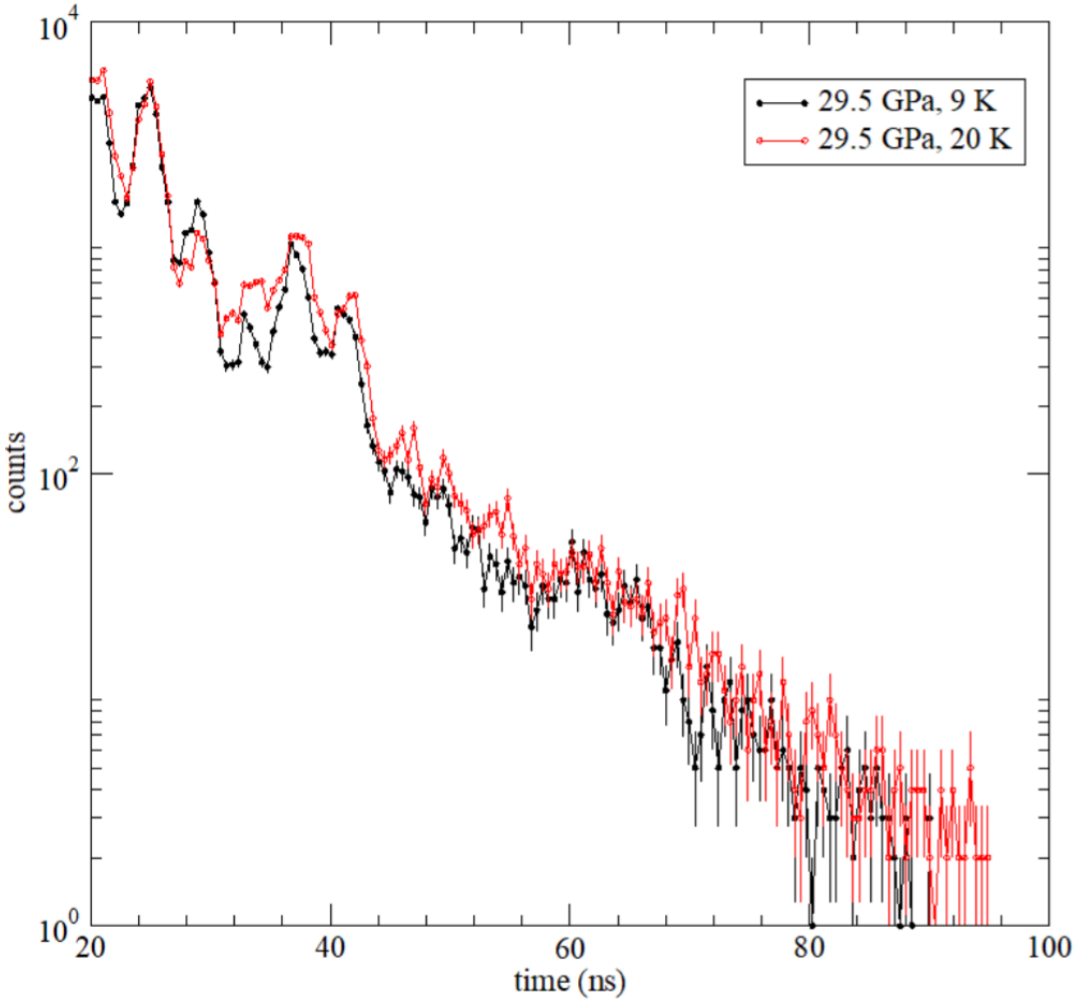

Fig. S13: Experimental SMS data at 29.5 GPa, for 9 K and 20 K. There is little to no temperature dependence on the signal, which indicates no magnetic transition between these temperatures.

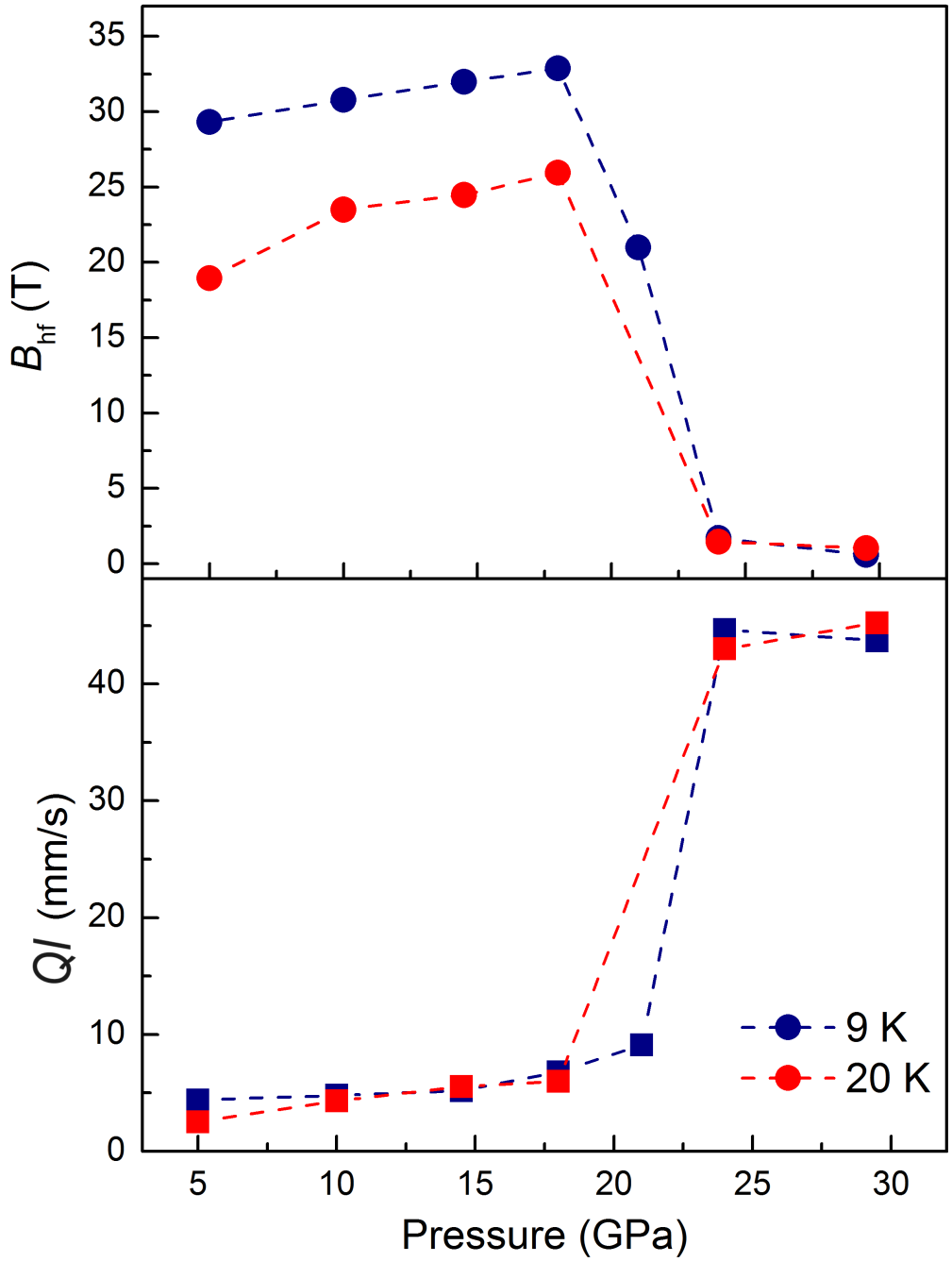

Fig. S14: Evolution of magnetic hyperfine field strength (top) and quadrupole interaction (bottom) as a function of pressure as extracted from SMS data using a model with paramagnetic interactions above 20 GPa.

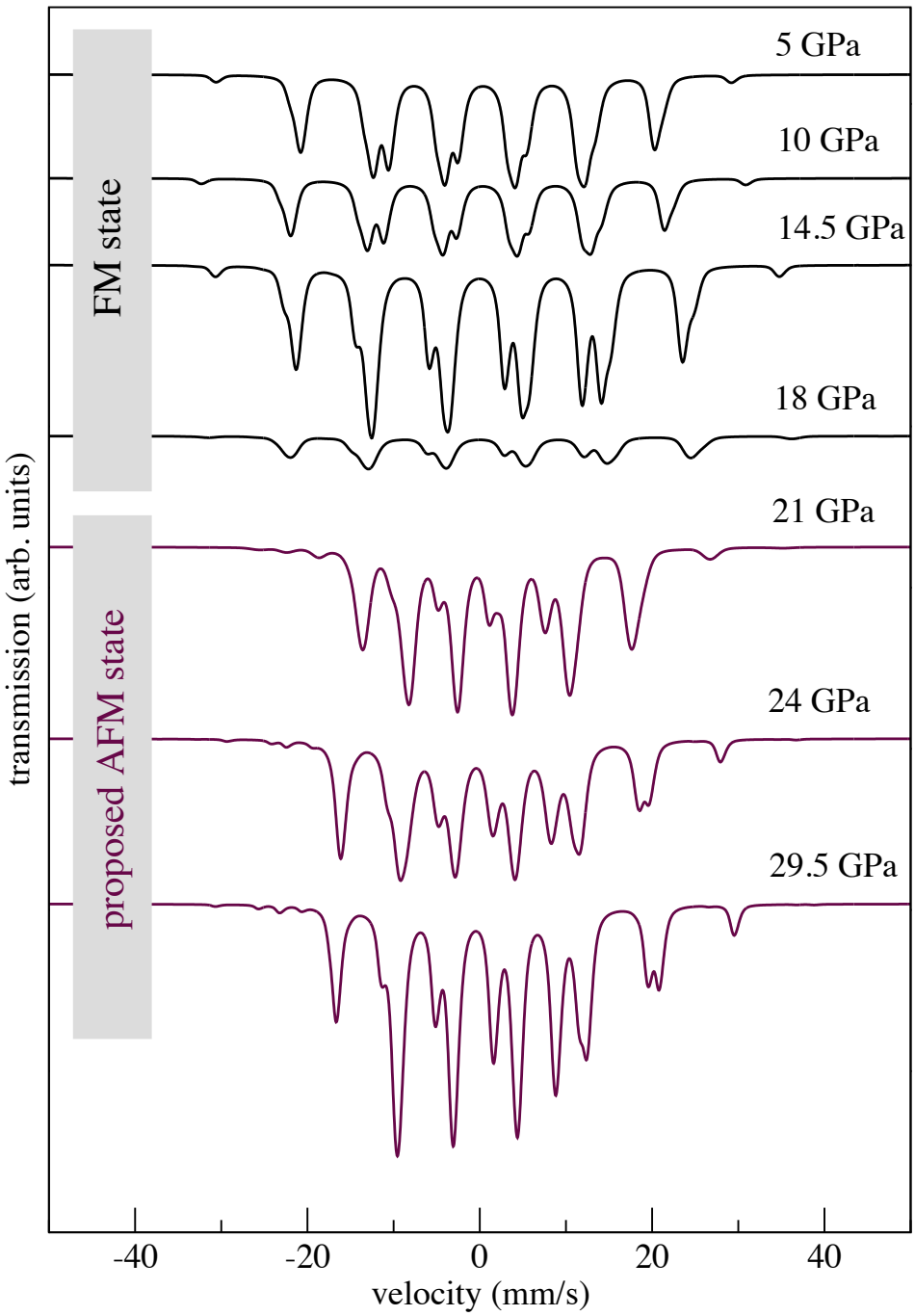

Fig. S15: Simulated energy domain spectra equivalent to the time domain SMS spectra for Model 1.The isomer shift is set to zero in the simulated spectra.